nature physics

ARTICLES

https://doi.org/10.1038/s41567-020-0923-8

Multi-scale spatial heterogeneity enhances particle clearance in airway ciliary arrays

Guillermina R. Ramirez-San Juan[1,2], Arnold J. T. M. Mathijssen[2], Mu He[3], Lily Jan[1,3,4], Wallace Marshall[1] and Manu Prakash[2]✉

Mucus clearance constitutes the primary defence of the respiratory system against viruses, bacteria and environmental insults. This transport across the entire airway emerges from the integrated activity of thousands of multiciliated cells, each containing hundreds of cilia, which together must coordinate their spatial arrangement, alignment and motility. The mechanisms of fluid transport have been studied extensively at the level of an individual cilium, collectively moving metachronal waves and, more generally, the hydrodynamics of active matter. However, the connection between local cilia architecture and the topology of the flows they generate remains largely unexplored. Here, we image the mouse airway from subcellular (nm) to organ (mm) scales, characterizing quantitatively its ciliary arrangement and the generated flows. Locally, we measure heterogeneity in both cilia organization and flow structure, but, across the trachea, fluid transport is coherent. To examine this result, a hydrodynamic model was developed for a systematic exploration of different tissue architectures. Surprisingly, we find that disorder enhances particle clearance, whether it originates from fluctuations, heterogeneity in multiciliated cell arrangement or ciliary misalignment. This resembles elements of 'stochastic resonance', in the sense that noise can improve the function of the system. Taken together, our results shed light on how the microstructure of an active carpet determines its emergent dynamics. Furthermore, this work is also directly applicable to human airway pathologies, which are the third leading cause of deaths worldwide.

The many functions of the airway are reflected by the variety of specialized cell types it contains, including multiciliated, secretory, nerve, immune and basal cells[1,2]. This inevitably leads to constraints in the organization of the airway cilia, which is compounded over several orders of magnitude[3,4] (Fig. 1a). Previous studies have noted the heterogeneity in airway cilia arrangement[5,6], but they lack quantitative descriptions of disorder across all relevant spatial scales (nm to mm).

Patterning and alignment of airway cilia across the scales

To quantitatively map the airway architecture across these scales, we imaged transgenic mice expressing a fluorescently tagged version of centrin (multiciliated-cell, basal-body-specific marker; see 'Tissue imaging' section in the Methods). Along the distal–proximal (D–P, lung–oral) axis of the trachea, multiciliated cells cover only a fraction of the surface, corresponding to $\bar{\varphi} = 0.37 \pm 0.02$, giving rise to a 'patchwork' pattern of regions with beating cilia and areas devoid of cilia (Fig. 1b and Extended Data Fig. 1a). Multiciliated cells are distributed uniformly along the D–P axis, except at the cartilage rings where their coverage fraction decreases (Fig. 1d).

To characterize the structure of the multiciliated cell pattern, we calculated its spatial correlation function $S_2(R)$ (see 'Measurement of cilia coverage fraction and wavelength from fixed samples' section in the Methods). We extracted two relevant length scales of the multiciliated cell pattern from this function: the characteristic diameter of a cell, $\rho = 8.4 \pm 1.7\,\mu$m (the first local minimum of S_2), and the wavelength of the pattern, $\lambda = 16 \pm 3.8\,\mu$m (the first local maximum), which corresponds to approximately two cell diameters (Fig. 1g). Furthermore, by analysing time-lapse videos of living tissue (Supplementary Video 1) we confirmed that the area fraction where cilia beat actively is indeed $\bar{\varphi} = 0.43 \pm 0.05$. Similarly, the wavelength measured from live trachea imaging, $\lambda = 22.8 \pm 3.9\,\mu$m, agrees with values obtained from fixed tissues (Extended Data Fig. 1c,d and Methods section 'Measurement of cilia coverage fraction and wavelength from live samples').

Each multiciliated cell is decorated with tens to hundreds of cilia (Fig. 1f)[4,7]. Quantification of the number of basal bodies from images of fixed trachea segments (Fig. 1c and Methods section 'Analysis of number and orientation of cilia') showed that each multiciliated cell has, on average, $\langle N \rangle = 169 \pm 61$ cilia. We note that this number fluctuates between 20 and 350 cilia per cell (Fig. 1f).

Individual cilia beat with an asymmetric wave form that is confined to a plane[8–10]. The direction of the active stroke of a cilium is determined by the relative orientation of the structures that anchor the cilium to the cell membrane. Thus, the beating plane of a cilium is defined uniquely by the relative orientation of the basal body[4], which in our experiments we marked with centrin, and its basal foot, which we marked with centriolin[11]. This polarity is established during organismal development through cytoskeletal rearrangements and hydrodynamic interactions, and becomes fixed at adulthood[4,12,3].

Therefore, to quantify the orientation of each cilium, i, we establish its polarity unit vector $\mathbf{p}_i$ by connecting the relative positions of its centrin and centriolin puncta (Fig. 1e, right, green arrows; Extended Data Fig. 1b and Methods section 'Analysis of number and orientation of cilia'). Subsequently, to define the average orientation of cilia within a given cell, for each multiciliated cell j we average its cilia vectors and denote the cellular-scale polarity by the unit vector $\mathbf{P}_j$ (Fig. 1e, left, magenta arrows). From these vectors we observe that cilia exhibit significant fluctuations in their relative

[1]Department of Biophysics and Biochemistry, University of California, San Francisco, CA, USA. [2]Department of Bioengineering, Stanford University, Stanford, CA, USA. [3]Department of Physiology, University of California, San Francisco, CA, USA. [4]Howard Hughes Medical Institute, University of California, San Francisco, CA, USA. ✉e-mail: manup@stanford.edu

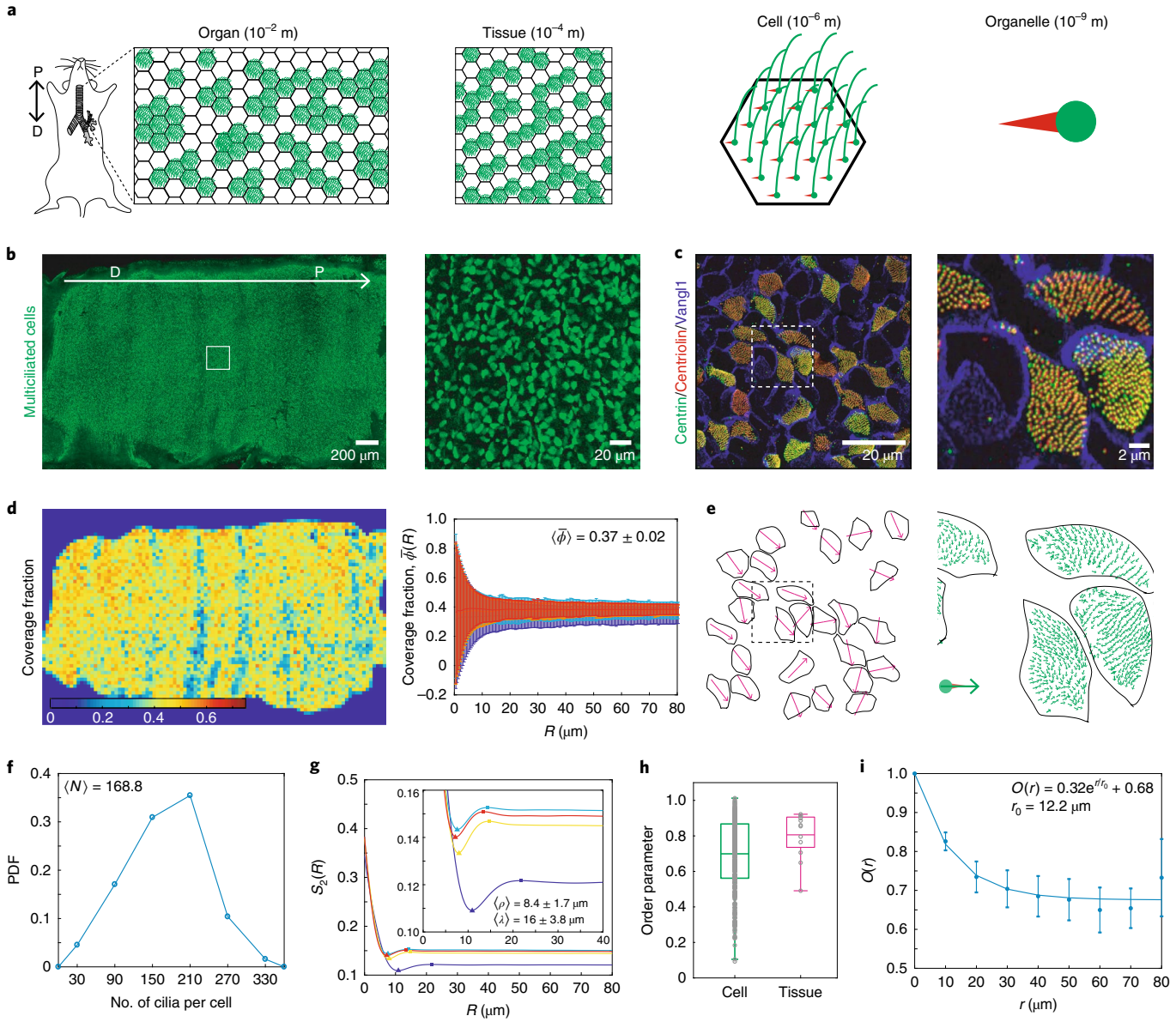

Fig. 1 | Heterogeneity in spatial patterning of cilia in the mouse airway epithelium. a, Schematic of the organization of multiciliated cells across spatial scales. Thousands of multiciliated cells line the trachea, forming a 'patchwork' pattern at the tissue scale. Each multiciliated cell contains hundreds of cilia anchored to the cell by the basal body. **b**, Left: fluorescence image of an entire trachea with multiciliated cells labelled with centrin-GFP. The arrow indicates the direction of fluid transport, from distal (D) to proximal (P) (lung → oral). Right: magnification of the region outlined by the white square in the left image. **c**, Left: fluorescence image of a section of the multiciliated epithelium. Vangl1 localizes to cell membranes. Fluorescently labelled centrin and centriolin mark individual basal bodies. The vector that connects centriolin → centrin defines the orientation of an individual cilium. Right: magnification of the region outlined by the white square in the left image. **d**, Left: heatmap of the coverage fraction of multiciliated cells ($\bar{\varphi}$). Right: coverage fraction measured in circular non-overlapping windows of radius R, uniformly distributed along the trachea. $\langle\bar{\varphi}\rangle$ is the average over all R and all tracheas imaged. Error bars represent s.d. **e**, Left: tissue-scale orientation field obtained by averaging the orientation of cilia within each multiciliated cell shown in **c**. Right: orientation of individual cilia shown in **c**. **f**, Probability density function (PDF) of the number of cilia measured in 375 multiciliated cells. **g**, Plot of the spatial correlation function, S_2, of the pattern of multiciliated cells. Inset: magnified region where the minima and maxima of $S_2(R)$ occur. Triangles mark the minimum, which corresponds to the typical diameter of a cell ρ, while squares mark the maximum, which corresponds to the wavelength of the patchwork pattern, λ. **h**, Orientational order parameter m calculated for multiciliated cells (green) and tissue-scale orientational order parameter M (magenta). The boxplot centre line indicates the mean, and the bottom and top edges of the box indicate the 25th and 75th percentiles, respectively. The whiskers extend to the most extreme data points. **i**, Spatial correlation function of the cellular-scale orientation $O(r) = \langle\mathbf{P}_j \cdot \mathbf{P}_{j+r}\rangle$. The orientation of cilia in the jth cell is compared to the orientation in the cells that are at a distance less than or equal to r. Points show the average measured values, and the solid line is the exponential fit. Error bars represent the s.e.m.

orientation, both across the tissue and within individual cells. These fluctuations are quantified by the order parameter $m = |\langle\mathbf{p}_i\rangle|$, analogous to magnetization. We find an average order parameter of $\langle m\rangle = 0.67 \pm 0.2$, representing the orientational heterogeneity at the subcellular scale. At the tissue scale the order parameter is $M = |\langle\mathbf{P}_j\rangle|$, where the average is taken over all cells in a field of view.

Here, we find that $\langle M\rangle = 0.80 \pm 0.13$, with small variations across different tissue sections (Fig. 1h). To determine how the orientation of cilia varies across neighbouring cells in the tissue, we compute the spatial correlation function, $O(r) = \langle \mathbf{P}_j \cdot \mathbf{P}_{j+r}\rangle$, where $\mathbf{P}_j$ is the orientation vector of the jth cell and $\mathbf{P}_{j+r}$ are the orientation vectors of all the cells found a distance less than or equal to r from the jth cell. (Fig. 1i and Methods section 'Analysis of number and orientation of cilia'). Interestingly, this function decays to its minimum value with a characteristic length scale of $r_0 = 12.2\,\mu$m, which corresponds approximately to one cell diameter, showing that cells are only aligned with their immediate neighbours. However, because the correlation function does not decay to zero, all cells in the tissue are still correlated globally. Altogether, these results show that heterogeneity is a feature of the spatial organization of airway cilia from the subcellular to the organ scale.

Ciliary flows are globally coherent but locally heterogeneous

Perfectly aligned and densely covered ciliary arrays will generate directed flows[13], but our results show that the trachea inherently features patchiness and misalignment (Fig. 1). In particular, this patchy architecture raises the key question of how particle transport is connected over regions devoid of cilia. Thus, we next investigated the flows generated by multiciliated cells in the trachea.

To monitor flow structure, fluorescent beads were added to the media as tracer particles. We find that flows across entire tracheas are coherent and globally directed along the D–P axis (Fig. 2a,c, left, Extended Data Fig. 2a and Supplementary Video 2) with an average speed of $(8.4 \pm 2.6)\,\mu$m s^{-1} (Fig. 2e). However, at a scale comparable to the wavelength of the multiciliated cell 'patchwork' pattern, $\lambda = 16 \pm 3.8\,\mu$m, we observe variations in the local flow direction and magnitude (Fig. 2a,c, right, Extended Data Fig. 2b and Supplementary Video 3). Specifically, we see connected regions with stronger flow, separated by regions of weaker flows. To quantify the structure of these currents we calculate the spatial ($\delta C_{vv}(R)$) and temporal ($\delta C_{vv}(\tau)$) correlations (Methods section 'Analysis of flows'). For each of our measurements, the decay of $\delta C_{vv}(R)$ can be fitted well by an exponential with an oscillatory component, $\delta C_{vv}(R) = A\mathrm{e}^{(-R/R_0)}\cos(wR) + \kappa$ (Extended Data Fig. 2e), which defines the correlation length R_0. Thus, the domain size of the correlated flow is $R_0 = 14.6 \pm 6.4\,\mu$m (Fig. 2h), comparable to the wavelength λ of the multiciliate cell pattern. Moreover, the timescale of temporal decorrelation, $\tau = 0.019 \pm 0.01$ s (Extended Data Fig. 2d) has the same order of magnitude as the timescale of the cilia beat frequency, CBF $= 11.8 \pm 2.3$ Hz (Extended Data Fig. 2c and Supplementary Video 4). Therefore, the spatio-temporal flow structure coincides with the spatio-temporal organization of the heterogeneous ciliary carpet.

To understand how globally directed flows emerge from micrometre-scale fluctuations, we developed a hydrodynamic model inspired by the 'envelope approach' introduced by Lighthill and Blake (Methods section 'Simulation'). Using a computational fluid dynamics (CFD) solver, we simulate the ciliary flows of the liquid film covering the epithelium (Fig. 3a). As the boundary condition input, we use the experimentally measured global and local tissue configurations (Fig. 2b). Specifically, the multiciliated cells are represented by a slip velocity U imposed at the tissue surface, while a no-slip condition is set in the absence of cilia. Hence, we compute the three-dimensional (3D) flow structure at different scales.

In agreement with our experiments, the simulated flows also show globally coherent currents directed across the trachea, but at the micrometre scale we see heterogeneity in the magnitude and direction of the flows (Fig. 2d). Comparison of the statistical properties of simulated and measured flows shows that the flow velocity distributions and their correlation lengths also agree, establishing the validity of our model (Fig. 2e–h and Extended Data Fig. 2f).

Flow structure is determined by multiciliated cell architecture

Importantly, our measurements of the flow generated by multiciliated cells in the trachea show that complete orientational order and coverage are not a requirement for a ciliary carpet to generate directed fluid flows. However, it is unclear how much variability in multiciliated cell configuration can be tolerated before fluid transport is impaired. Therefore, we next use our model to uncover how controlled changes in the spatial distribution of multiciliated cells impact the properties of the flow they generate (Fig. 3a,b).

We explore systematically how total flux and particle clearance time change as a function of variations in multiciliated cell coverage fraction, wavelength, and orientational and geometrical order. The total flux $J = \int v_x \mathrm{d}y\mathrm{d}z$ measures the strength of the flow $\mathbf{v}(\mathbf{r})$ globally. To account for the local flow microstructure, we compute the mean first-passage time $\langle T\rangle$ taken to travel a distance L along x for an ensemble of particles advected by the flow (Methods section 'Total flux and clearance time'). These particles could represent viruses, bacteria or other pathogens that are cleared by the ciliary carpet. This first-passage time is a measure of streamline connectivity, thus flow topology, rather than only flow strength.

First, we test the role of coverage fraction on flow architecture. We observe that the total flux generated by the ciliary carpet increases linearly with coverage fraction (Fig. 3c, right). In the limit of low coverage ($\varphi \to 0$) the flow structure features recirculating eddies, approaching the Stokeslet flow due to a point force confined in a liquid film (Methods section 'Fundamental solution' and Extended Data Figs. 3 and 4). As the coverage fraction grows, regions of negative flux disappear and, in the limit $\varphi \to 1$, a uniform flow is recovered. Consequently, the clearance time (red stars) increases at low φ, as expected, but not linearly. A reduction of coverage therefore strongly impacts flow strength.

We then vary the periodicity of the multiciliated cell pattern. We define the 'patchiness' as the dimensionless number λ/H, where λ is the wavelength of the multiciliated cell pattern and H is the height of the fluid film. We keep the coverage fraction and film height constant, distributing the same amount of multiciliated cells in clusters of different sizes (green arrows), varying only the wavelength λ (Fig. 3d). The total flux J is constant for all configurations, because the total force exerted on the liquid is the same. However, the streamline structure changes as a function of multiciliated cell arrangement. For large patchiness, recirculating eddies emerge that create zones where particles are trapped in closed streamline orbits (dashed purple separatrices). However, when cells are distributed more homogeneously, these zones disappear and consequently clearance times are reduced (Fig. 3d). We note that the emergence of recirculation zones can be tuned independently by reducing the film height. Therefore, higher patchiness caused either by dehydration of the liquid film or long wavelengths leads to impaired clearance.

Disorder can enhance particle transport

Having examined how deterministic parameters of multiciliated cell organization influence flow structure, we now analyse the impact of introducing disorder in these ciliary arrays. Surprisingly, we find that different types of disorder can improve clearance.

In the trachea, patches of multiciliated cells lack crystalline order (Fig. 1b,d). We introduce this geometric heterogeneity by shifting the positions of ciliated patches along x and y with standard deviation σ. Thus, geometric heterogeneity is described by the order parameter $\gamma = 1 - \frac{\sigma\sqrt{2}}{\lambda}$, the crystallinity. The resulting flows (Fig. 4a) again feature a constant total flux but, importantly, the geometric disorder breaks open the closed orbits, causing streamlines to cut through the recirculation zones (black dashed streamlines) and strongly reducing clearance time $\langle T\rangle$.

Next, we examine disorder in the cilia orientations (Fig. 1h) by varying the orientational order parameter $\langle p_x\rangle = M$ (Fig. 4b).

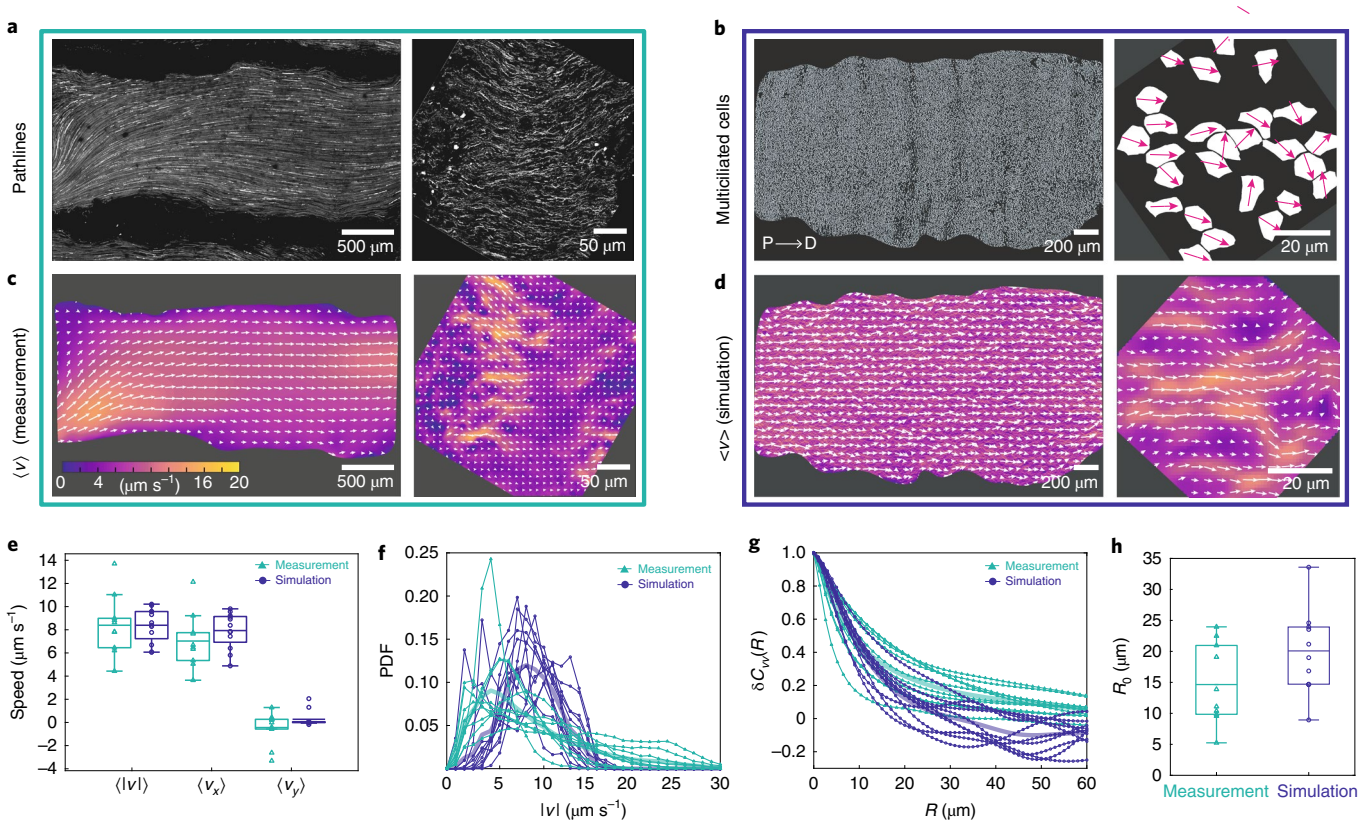

Fig. 2 | Measurements of ciliary flows at the tissue and cellular scales. a, Left: pathlines of the flow generated by multiciliated cells across the entire trachea. Right: pathlines of the flow visualized at a scale comparable to the wavelength of the cilia patchwork pattern. **b**, Binary images obtained by thresholding the images of multiciliated cell localization shown in Fig. 1b,c. White regions represent multiciliated cells. Magenta arrows show the average orientation of cilia within each multiciliated cell measured from Fig. 1c. These coverage and orientation fields are used as input for the model, shown in **d**. **c**, Representative experimental flow fields measured at the scale of the entire trachea (left) and with micrometre resolution (right). Colours show the flow velocity magnitude and white arrows indicate the streamlines. **d**, Simulated flow fields, using the experimental data of **b** as input. Colours show the flow velocity magnitude and white arrows indicate streamlines. **e**, Comparison of flow speeds between the experiment (green) and model (blue). The majority comes from the *x* component. Boxplot central lines indicate the mean, and the bottom and top edges of the box indicate the 25th and 75th percentiles, respectively. The whiskers extend to the most extreme data points not considered outliers. **f**, PDFs of the flow speed, PDF($\langle|v|\rangle$) from the experiment and model. Thin lines show the PDF from a field of view of the size shown in **c** and **d** (right). Thick lines are the average of all flow fields analysed. **g**, Comparison of the spatial autocorrelation function between experiment and model. Thin lines show measurements from a field of view of the size shown in **c** and **d** (right). **h**, Comparison of correlation length R_0 from the experiment, $\langle R_0\rangle = 14.6 \pm 6.4\,\mu$m, and from the simulation, $\langle R_0\rangle = 20 \pm 6.8\,\mu$m. Boxplot central lines indicate the mean, and the bottom and top edges of the box indicate the 25th and 75th percentiles, respectively. The whiskers extend to the most extreme data points not considered outliers.

The total flux is no longer conserved and decreases with orientational noise. Interestingly, we observe a biphasic behaviour in clearance time: for weakly misaligned cilia the recirculation zones are broken up and the clearance time is reduced, but the clearance time increases for strong misalignment. We predict an optimum around $M = 0.89 \pm 0.06$ (black arrow). Looking back at the measured value, $M = 0.81 \pm 0.12$ (Fig. 1h), we see that the mouse tracheas occupy the same region in this parameter space.

Finally, we study the effect of diffusion, D, which can be due to thermal or ciliary beating noise (Supplementary Video 5). To understand how diffusion impacts particle clearance, we compare the advection time $\tau_a = \lambda/(\varphi U)$ with the diffusion time $\tau_d = \lambda^2/D$ required for particles to escape eddies of size $\varepsilon \approx \lambda$. The ratio of these times defines the Péclet number, $\mathrm{Pé} = \tau_d/\tau_a = \varphi\lambda U/D$, and their sum gives the mean clearance time, $\langle T\rangle \approx \tau_d + \tau_a$. Therefore, with weak fluctuations ($\mathrm{Pé} \gg 1$) the particles remain stuck in closed orbits (Fig. 4c, left), but strong diffusion ($\tau_d \to 0$) reduces clearance times by helping particles escape and connecting regions of closed streamlines (Fig. 4c, right). We note that diffusion only reduces clearance time in carpets with closed eddies, for example at high patchiness, because $\tau_d = 0$ for all values of Pé in the absence of recirculation zones.

To verify the robustness of these results, we extended our simulations to a non-Newtonian fluid with a shear-dependent viscosity (Methods section 'Shear-dependent viscosity' and Extended Data Fig. 5), and we also control for different ciliary array cell structures (Methods section 'Hexagonal arrays' and Extended Data Fig. 6). Closed streamline areas still appear at high patchiness, both in shear-thinning and shear-thickening fluids, leading to long clearance times due to particle recirculation. We find that, for these flow structures, clearance can still be reduced by disorder.

To cast our results in a broader context, we map the phase space of clearance times in terms of ciliary organization (Fig. 4d). First, we observe that for a large range of coverage fractions ($\varphi \gtrsim 0.58$) the clearance time is minimal. Surprisingly, the mouse airway operates below this ideal regime, but its low patchiness and moderate disorder in cilia orientation still allow for clearance times to be relatively small. This observation raises the question of whether airway tissues from other animals have similar, sub-optimal, coverage fractions. A brief literature survey showed that different species have

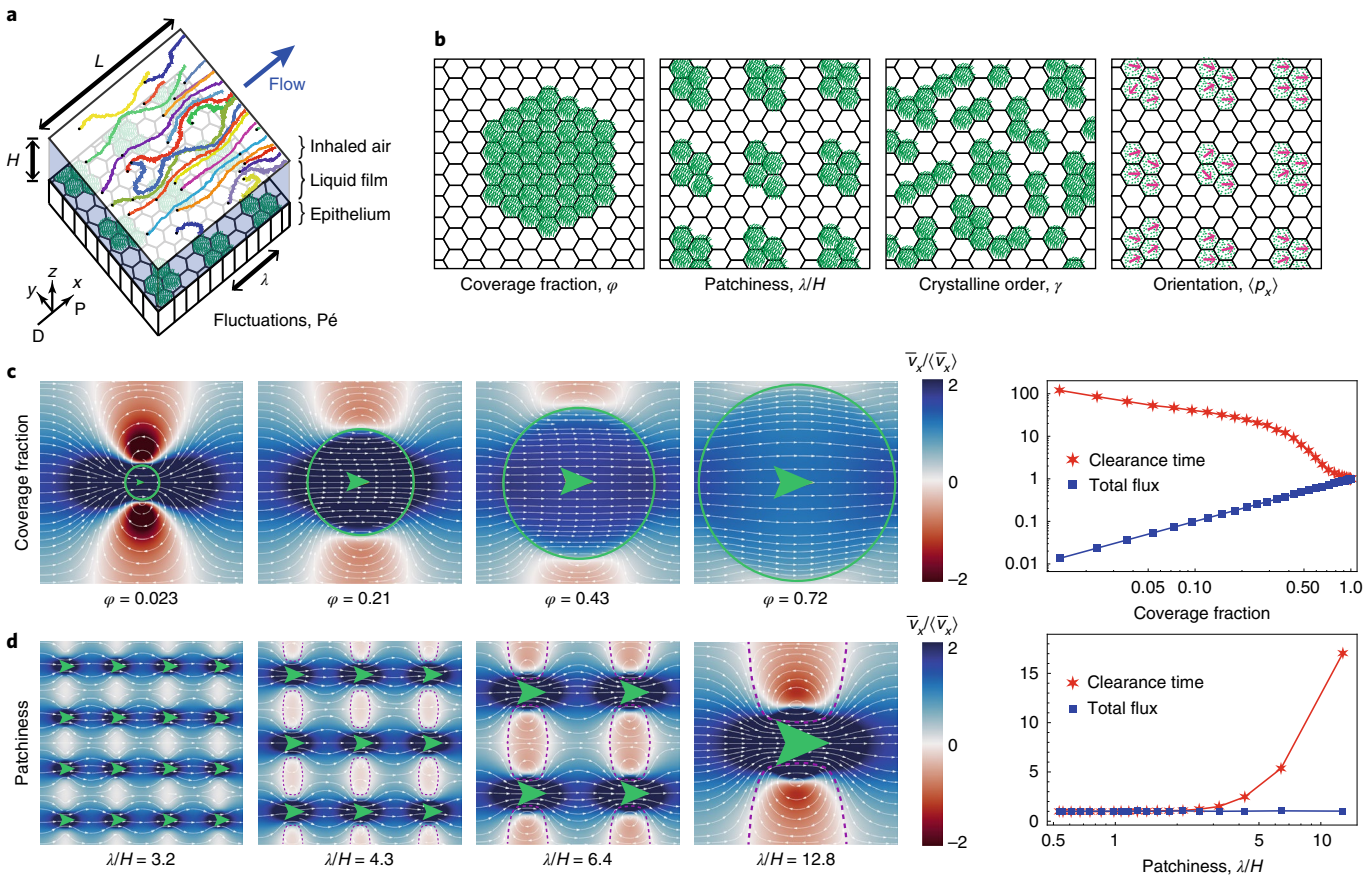

Fig. 3 | Hydrodynamic model for particle flux and clearance. a, Diagram of the simulation geometry. A pattern of multiciliated cells (green) drives a liquid film flow (blue) in a 3D CFD simulation with periodic boundary conditions in x and y. Particle trajectories with random initial positions are subject to this flow and fluctuations. **b**, Total flux and clearance times are examined as a function of ciliary organization, characterized by the coverage fraction φ, wavelength λ, crystallinity γ and orientation order $\langle p_x \rangle$. **c**, Higher coverage fractions improve clearance. Left images: streamlines (white) and the longitudinal flow strength (red–blue) as a function of coverage fraction φ. Green circles indicate the area covered by cilia and green arrows their orientation. Right: corresponding plot of clearance time and total flux, normalized with respect to full coverage, showing the mean of an ensemble of $N_p = 10^4$ particle trajectories. **d**, Patchiness induces recirculation and slows clearance. Left: flows as a function of wavelength λ. Dashed purple lines are separatrix streamlines that isolate recirculation zones (red) from the main currents (blue). Right: corresponding clearance time and flux, normalized with respect to uniform coverage, again averaged over $N_p = 10^4$ particle trajectories.

similar coverage fractions and patchiness (Extended Data Fig. 7), clustering in the same region of the phase diagram as the mouse (Fig. 4). Snakes are an exception, potentially because of their unique trachea morphology. Given that patchiness is conserved among organisms with drastically different trachea lengths, we conjecture that maintaining this number fixed among different species provides an effective mechanism for clearance. However, further studies comparing the morphology of tracheas in large sets of images for every species will be required to understand whether this design principle is universal.

Discussion

The emergence of spatio-temporal patterns is a feature central to flow generation in multiciliated tissues[14–16]. Previous studies have focused on how temporal cooperative behaviours, such as the formation of metachronal waves, influence fluid transport[17–21]. However, the connection between spatial patterning and fluid transport have remained unknown. Our work establishes a quantitative link between the topology of the flow generated by a ciliary array and its underlying spatial organization. We investigate the arrangement of cilia and their associated flow generation, from the molecular to the organ scale, in the mouse conductive airway. Using a hydrodynamic model, we explore the effect of varying ciliary arrangements on flow structure. We find that while patchiness due to spatial constraints generally reduces streamline connectivity, a moderate amount of disorder can enhance particle clearance. This beneficial disorder can arise from heterogeneity in the ciliary arrangement, ranging from the patterning and alignment of individual cilia up to the arrangement of multiciliated cells in the entire trachea. Similarly, thermal noise and fluctuations in cilia activity including enhanced diffusion due to flows near beating cilia[22] could decrease the effective Péclet number and hence reduce clearance times. Therefore, particle clearance in the airway is not necessarily proportional to the overall liquid flux, but rather set by streamline connectivity.

Even if surprising, it is not uncommon in physical and biological systems that ‘noise’ can prove advantageous, a concept sometimes referred to as stochastic resonance[23–25]. In these systems noise levels are initially beneficial but often only up to a point, the resonance peak, after which more fluctuations become unfavourable[23]. The organization of cilia should be understood in this context of trade-offs in self-assembled systems. Indeed, across diverse physiological contexts, disorder in the spatio-temporal organization of cilia can be harnessed to optimize their biological function. For example, dynamic switches in beating patterns modulate the transport of cerebrospinal fluid[26], length differences

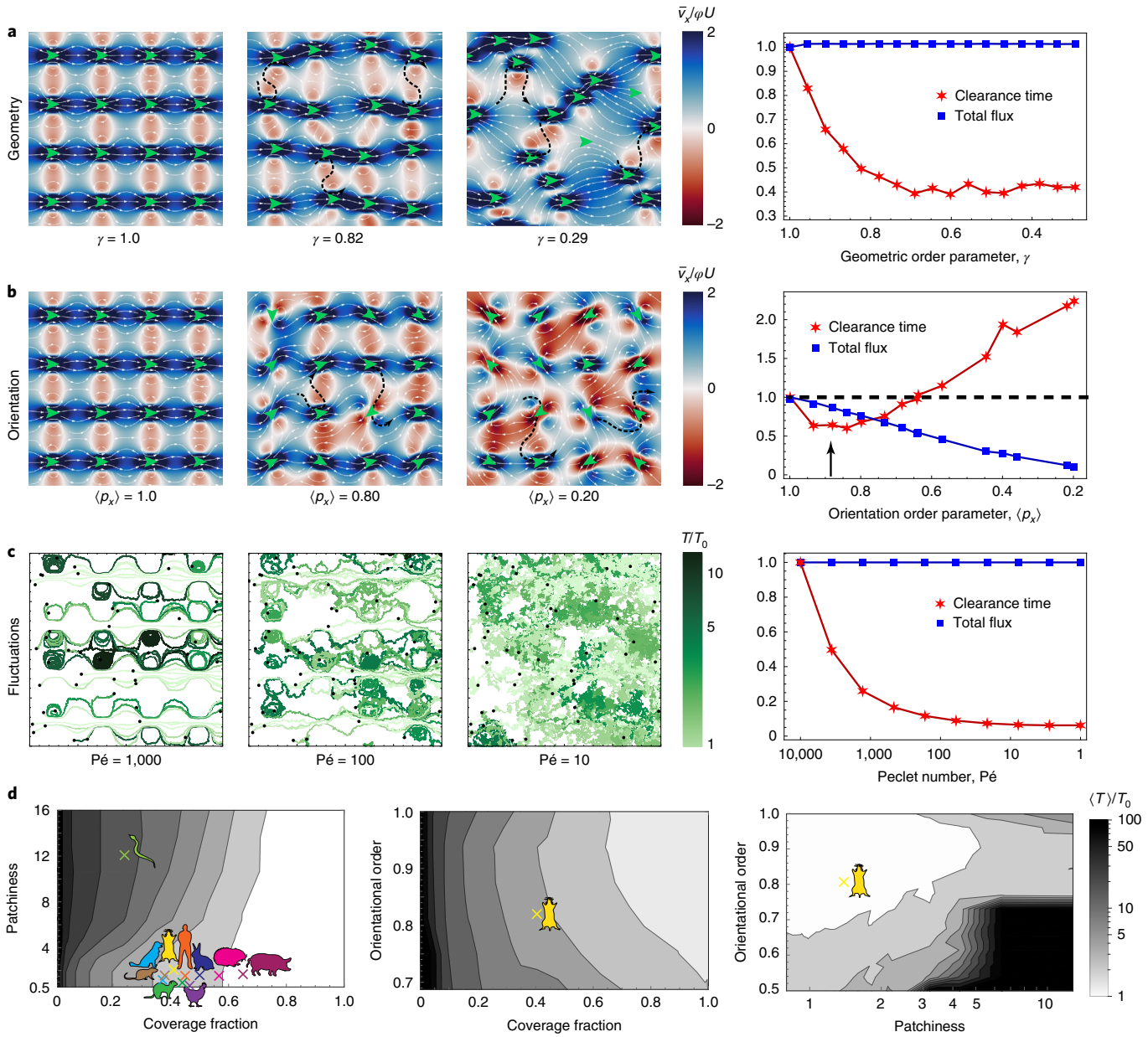

Fig. 4 | Disorder improves clearance in heterogeneous epithelia. a, Left: flow strength along the D–P axis (red–blue) and streamlines (white) as a function of crystallinity γ. Green arrows indicate the position and orientation of the cilia patches. A few typical (black dashed) streamlines are shown to cross through recirculation areas. Right: corresponding total flux and clearance time, normalized with respect to crystalline order. $N_p = 10^3$ particle trajectories. **b**, Flow and clearance as a function of cilia orientational order $\langle p_x \rangle$. Same as **a** otherwise. **c**, Left: particle trajectories subject to flow and diffusion for a range of Péclet numbers, Pé $= \lambda\varphi U/D$. Right: corresponding total flux and clearance time, normalized with respect to weak fluctuations. $N_p = 10^4$ particle trajectories. **d**, Phase diagrams showing clearance time (greyscale, defined in the key) for the combinations of (φ, λ/H, M), with constant $M = 1$, $\lambda/H = 8$ and $\varphi = 0.4$, respectively. The mouse cartoon indicates the measurements for the mouse epithelium. Other coloured cartoons in the first panel show values of patchiness and coverage fraction measured for several different animals, from data available in the literature (see Methods section 'Literature survey of patchiness and coverage fraction' and Extended Data Fig. 7).

can create hydrodynamic microhabitats[27], and topological defects can enhance feeding in starfish larvae[28] and attract nutrients to active carpets[29].

However, disorder can also be detrimental to physiology, as reduced ciliary coverage and alignment are a hallmark of airway pathologies[30,31]. Our phase diagrams (Fig. 4d) provide a framework to understand how much heterogeneity can be tolerated before clearance times increase beyond a critical value. Understanding the link between ciliary organization and flow structure could open up new avenues for diagnostics and therapies for airway pathologies.

Beyond understanding airway physiology, our phase diagrams (Fig. 4d) prescribe the design principles for synthetic active carpets. This could open new doors to fabricate active surfaces that drive fluid flows with programmable and adaptive topologies, with diverse engineering applications including microseparation and cellular rheometry.

Online content

Any methods, additional references, Nature Research reporting summaries, source data, extended data, supplementary information,

acknowledgements, peer review information; details of author contributions and competing interests; and statements of data and code availability are available at https://doi.org/10.1038/s41567-020-0923-8.

Received: 7 June 2019; Accepted: 28 April 2020;
Published online: 08 June 2020

References

1. Fahy, J. V. & Dickey, B. F. Airway mucus function and dysfunction. *New Engl. J. Med.* **363**, 2233–2247 (2010).
2. Plasschaert, L. W. et al. A single-cell atlas of the airway epithelium reveals the CFTR-rich pulmonary ionocyte. *Nature* **560**, 377–381 (2018).
3. Vladar, E. K., Bayly, R. D., Sangoram, A. M., Scott, M. P. & Axelrod, J. D. Microtubules enable the planar cell polarity of airway cilia. *Curr. Biol.* **22**, 2203–2212 (2012).
4. Marshall, W. F. & Kintner, C. Cilia orientation and the fluid mechanics of development. *Curr. Opin. Cell Biol.* **20**, 48–52 (2008).
5. Francis, R. J. B. et al. Initiation and maturation of cilia-generated flow in newborn and postnatal mouse airway. *Am. J. Physiol. Lung Cell. Mol. Physiol.* **296**, L1067–L1075 (2009).
6. Holley, M. C. & Afzelius, B. A. Alignment of cilia in immotile-cilia syndrome. *Tissue Cell* **18**, 521–529 (1986).
7. Nanjundappa, R. et al. Regulation of cilia abundance in multiciliated cells. *eLife* **8**, e44039 (2019).
8. Sleigh, M. A., Blake, J. R. & Liron, N. The propulsion of mucus by cilia. *Am. Rev. Resp. Dis.* **137**, 726–741 (1988).
9. Chilvers, M. A. & O'Callaghan, C. Analysis of ciliary beat pattern and beat frequency using digital high speed imaging: comparison with the photomultiplier and photodiode methods. *Thorax* **55**, 314–317 (2000).
10. Shinohara, K. et al. Absence of radial spokes in mouse node cilia is required for rotational movement but confers ultrastructural instability as a trade-off. *Dev. Cell* **35**, 236–246 (2015).
11. Herawati, E. et al. Multiciliated cell basal bodies align in stereotypical patterns coordinated by the apical cytoskeleton. *J. Cell Biol.* **214**, 571–586 (2016).
12. Mitchell, B., Jacobs, R., Li, J., Chien, S. & Kintner, C. A positive feedback mechanism governs the polarity and motion of motile cilia. *Nature* **447**, 97–101 (2007).
13. Liron, N. Fluid transport by cilia between parallel plates. *J. Fluid Mech.* **86**, 705–726 (1978).
14. Bruot, N. & Cicuta, P. Realizing the physics of motile cilia synchronization with driven colloids. *Ann. Rev. Condens. Matter Phys.* **7**, 323–348 (2016).
15. Brennen, C. & Winet, H. Fluid mechanics of propulsion by cilia and flagella. *Ann. Rev. Fluid Mech.* **9**, 339–398 (1977).
16. Eloy, C. & Lauga, E. Kinematics of the most efficient cilium. *Phys. Rev. Lett.* **109**, 038101 (2012).
17. Vilfan, A. & Jülicher, F. Hydrodynamic flow patterns and synchronization of beating cilia. *Phys. Rev. Lett.* **96**, 058102 (2006).
18. Brumley, D. R., Polin, M., Pedley, T. J. & Goldstein, R. E. Hydrodynamic synchronization and metachronal waves on the surface of the colonial alga *Volvox carteri*. *Phys. Rev. Lett.* **109**, 268102 (2012).
19. Elgeti, J. & Gompper, G. Emergence of metachronal waves in cilia arrays. *Proc. Natl Acad. Sci. USA* **110**, 4470–4475 (2013).
20. Guo, H., Nawroth, J., Ding, Y. & Kanso, E. Cilia beating patterns are not hydrodynamically optimal. *Phys. Fluids* **26**, 091901 (2014).
21. Feriani, L. et al. Assessing the collective dynamics of motile cilia in cultures of human airway cells by multiscale DDM. *Biophys. J.* **113**, 109–119 (2017).
22. Ding, Y., Nawroth, J. C., McFall-Ngai, M. J. & Kanso, E. Mixing and transport by ciliary carpets: a numerical study. *J. Fluid Mech.* **743**, 124–140 (2014).
23. McDonnell, M. D. & Abbott, D. What is stochastic resonance? Definitions, misconceptions, debates and its relevance to biology. *PLoS Comput. Biol.* **5**, e1000348 (2009).
24. Sagués, F., Sancho, J. M. & García-Ojalvo, J. Spatiotemporal order out of noise. *Rev. Mod. Phys.* **79**, 829 (2007).
25. Gammaitoni, L., Hänggi, P., Jung, P. & Marchesoni, F. Stochastic resonance. *Rev. Mod. Phys.* **70**, 223–287 (1998).
26. Faubel, R., Westendorf, C., Bodenschatz, E. & Eichele, G. Cilia-based flow network in the brain ventricles. *Science* **353**, 176–178 (2016).
27. Nawroth, J. C. et al. Motile cilia create fluid-mechanical microhabitats for the active recruitment of the host microbiome. *Proc. Natl Acad. Sci. USA* **114**, 9510–9516 (2017).
28. Gilpin, W., Prakash, V. N. & Prakash, M. Vortex arrays and ciliary tangles underlie the feeding-swimming trade-off in starfish larvae. *Nat. Phys* **13**, 380–386 (2017).
29. Mathijssen, A. J. T. M., Guzmán-Lastra, F., Kaiser, A. & Löwen, H. Nutrient transport driven by microbial active carpets. *Phys. Rev. Lett.* **121**, 248101 (2018).
30. Rayner, C. F. et al. Ciliary disorientation alone as a cause of primary ciliary dyskinesia syndrome. *Am. J. Resp. Crit. Care Med.* **153**, 1123–1129 (1996).
31. Armengot, M. et al. Nasal mucociliary transport and ciliary ultrastructure in cystic fibrosis. A comparative study with healthy volunteers. *Int. J. Pediatric Otorhinolaryngol.* **40**, 27–34 (1997).

Methods

Tissue imaging. *Mouse husbandry.* Arl13b-mCherry;centrin2-GFP mice (JAX 027967) were maintained in FVB/N background[32]. Mice imaged were at stage >p15, to ensure that patterning of multiciliated cells was fixed[5]. Mice were euthanized by cervical dislocation. All protocols were approved by the University of California San Francisco Institutional Animal Care and Use Committee.

Tissue staining. After euthanasia, tracheas (segments C1–C10 or C1–C12) were dissected and placed in ice-cold Dulbecco's modified Eagle medium: nutrient mixture F12 (DMEM/F12, Invitrogen). Tissues were sliced open along the P–D axis and fixed with ice-cold methanol for 10 min. After fixation, samples were washed three times (5–10 min each) and blocked (30–60 min) with IF buffer (1× PBS with 1% heat-inactivated goat/donkey serum and 0.3% Triton X-100). Tissues were incubated with primary antibodies (mouse monoclonal anti-centriolin, Santa Cruz, sc-365521, 1:500 dilution; rabbit anti-Vangl1, Sigma, HPA025235, 1:1,000 dilution) for 1 h at room temperature or overnight at 4 °C. Secondary antibodies used were Alexa Fluor 594 goat anti-rabbit and Alexa 633 donkey anti-mouse (Invitrogen, 1:1,000 dilution). Samples were mounted with Fluoromount-G (SouthernBiotech).

Microscopy and live-tissue imaging. For multiciliated cell imaging, whole-mount fixed trachea samples were imaged using a Zeiss LSM 780 laser scanning confocal microscope and a ×20 Plan Apo NA 0.8 air objective (Stanford Cell Sciences Imaging Facility).

For basal body imaging, fixed trachea segments stained with centriolin and Vangl1 antibodies were imaged using a Zeiss LSM 880 laser scanning confocal equipped with Airyscan and a ×40 Plan Neo NA 1.3 oil immersion objective (Gladstone Institutes Histology and Microscopy Core).

For flow imaging, fluorescent beads (FluoSpheres carboxylate-modified microspheres, 0.5 and 2 µm, Invitrogen) were added to the medium as tracer particles. Tracheas used for local flow imaging were cut into segments of 2–3 rings, while tracheas used for global flow imaging were left intact lengthwise. In all cases, tissues were sliced open along the P–D axis. Imaging was performed in an environmental chamber (5% CO_2 at 36 °C, Okolab) with an inverted microscope (Ti-E, Nikon) equipped with a confocal scan head (Andor Borealis CSU-W1), laser merge module 405, 488, 561 and 640 nm laser lines (Andor 4-line laser launch) and a Zyla 4.2 sCMOS camera (Andor, Oxford Instruments). Global flows were imaged using a ×4 Plan Apo NA 0.2 dry objective at 1 frame per second, while local flows were imaged with a ×40 Plan Apo LWD NA 1.5 water immersion objective at 18–30 frames per second.

For cilia live imaging, tracheas were cut into segments of 2–3 rings and sliced open along the P–D axis. Tissue pieces were mounted on a 35 mm glass-bottomed dish (MatTek, part no. P35G-0.170-14-C). Imaging was performed in an environmental chamber (5% CO_2 at 36 °C, Okolab) with an inverted microscope (Ti-E, Nikon) equipped with a light source (Sutter XL lamp), differential interference contrast (DIC) optics and ORCA-Flash4.0 V2 camera (Hamamatsu). Cilia were imaged with a ×40 DIC Plan Apo LWD NA 1.5 water immersion objective and a ×60 DIC Plan Apo VC NA 1.4 oil immersion objective.

Image analysis. *Measurement of cilia coverage fraction and wavelength from fixed samples.* Coverage fraction and wavelength were measured from 2D binarized images of the entire trachea obtain from multiciliated cell imaging. See Supplementary Section 1a for details.

Each binarized trachea image is described by the coverage fraction function:

$$I(\mathbf{r}) = \begin{cases} 1, & \text{if } \mathbf{r} \in \text{multiciliated cell} \\ 0, & \text{otherwise} \end{cases} \tag{1}$$

where $\mathbf{r}_i = (x_i, y_i)$ is the position of the ith pixel of the 2D image.

We compute the coverage fraction $\langle I(\mathbf{r})\rangle$ in N circular non-overlapping regions distributed uniformly over the entire image. Thus, the average coverage fraction for a given trachea is

$$\bar{\varphi}(R) = \frac{1}{N}\sum_{i=1}^{N}\langle I(\mathbf{r}_i)\rangle \tag{2}$$

where the average is taken over all the points in the circle of radius R centred at $\mathbf{r}_i$.

To measure the wavelength of the pattern, λ, we compute the spatial correlation function of I. For an image of size $m \times n$ this is defined as

$$\hat{S}_2(\mathbf{R}) = \langle I(\mathbf{r})I(\mathbf{r}+\mathbf{R})\rangle \tag{3}$$

A discretized version of this equation is given by

$$\hat{S}_2(x,y) = \frac{1}{N_2}\sum_{i=1}^{i_{\max}}\sum_{j=1}^{j_{\max}} I(i,j)I(i+x, j+y) \tag{4}$$

where $i_{\max} = m - i$, $j_{\max} = n - j$ and $N_2 = i_{\max} \times j_{\max}$. Given this 2D function $\hat{S}_2(x,y)$, we obtain the 1D isotropic correlation function $S_2(R)$ by averaging over the $\hat{S}_2(x,y)$ values at a fixed radius R.

We extract two length scales from this function. The first local minimum of S_2 occurs at the characteristic size of a cell, ρ, while the first local maximum of S_2 corresponds to the wavelength of the pattern, λ.

Measurement of cilia coverage fraction and wavelength from live samples. Coverage fraction $\bar{\varphi}$ and wavelength λ were measured from 2D binarized images where regions with white pixels correspond to regions of cilia activity. $\bar{\varphi}$ and λ were calculated as described in the previous section.

Analysis of number and orientation of cilia. The number of cilia corresponds to the number of basal bodies. Basal bodies were counted from centrin-GFP images as described in Supplementary Section 1c.

The orientation of a cilium is defined by the unit vector $\mathbf{p}_i$ that connects each basal body (centrin) with its corresponding basal foot (centriolin). For details on how $\mathbf{p}_i$ was obtained see Supplementary Section 1c.

The cellular-scale cilia organization was measured using the order parameter m:

$$m = |\langle \mathbf{p}_i \rangle| \tag{5}$$

where the average is taken over all cilia in a cell.

To measure tissue-scale cilia organization we calculate the order parameter M:

$$M = |\langle \mathbf{P}_j \rangle| \tag{6}$$

where $\mathbf{P} = \langle \mathbf{p}_i \rangle$ is a unit vector that represents the orientation of cilia within a cell, obtained by averaging the unit orientation vectors of all cilia within a cell.

To determine how the orientation of cilia varies across neighbouring cells, we compute the spatial correlation function of $\mathbf{P}$, defined as

$$O(r) = \langle \mathbf{P}_j \cdot \mathbf{P}_{j+r} \rangle \tag{7}$$

where $\mathbf{P}_j$ is the average orientation of cilia in the jth cell as defined by equation (M6) and $\mathbf{P}_{j+r}$ is the average orientation of cilia in the cells at a distance less than or equal to r. The average is taken over all the polarity vectors in an image.

Analysis of flows. Flow fields were obtained from time-lapse videos as described in the section 'Microscopy and live-tissue imaging'. Particle image velocimetry (PIV) fields were generated using 'mpiv'[33]. For details on PIV analysis and flow speed calculations see Supplementary Section 1d.

To characterize the temporal and spatial structure of the flow we calculate the spatial and temporal autocorrelations of the velocity fields averaged over 1 s, $\bar{\mathbf{v}}$. We subtract the spatial average from the velocity field, $\langle \bar{\mathbf{v}} \rangle$, and autocorrelate the velocity fluctuation field, defined as $\delta\bar{\mathbf{v}} = \bar{\mathbf{v}} - \langle \bar{\mathbf{v}} \rangle$. Thus the isotropic autocorrelation function is defined as

$$\delta C_{vv}(R) = \frac{\langle \sum_i \delta\bar{\mathbf{v}}(\mathbf{r}_i) \cdot \delta\bar{\mathbf{v}}(\mathbf{r}_i + \mathbf{R}) \rangle}{\langle \sum_i \delta\bar{\mathbf{v}}_i(\mathbf{r}_i) \cdot \delta\bar{\mathbf{v}}(\mathbf{r}_i) \rangle} \tag{8}$$

The sum is taken over all velocity fluctuation vectors in the field of view and the angle brackets indicate averaging over all directions.

To obtain the correlation length R_0, we fit an exponential function of the form $\delta C_{vv}(R) = Ae^{-R/R_0}\cos(wR) + \kappa$ to $\delta C_{vv}(R)$, where w, A and κ are fit constants with the constraint $A + \kappa = 1$.

To calculate the temporal correlation length we compute the temporal autocorrelation function of the velocity fluctuation field $\delta\mathbf{v}_i = \mathbf{v}(\mathbf{r}_i) - \langle \mathbf{v} \rangle$ where $\langle \mathbf{v} \rangle$ is the spatial average velocity vector at each time point t. The temporal autocorrelation function is defined as

$$\delta C_{vv}(\tau) = \frac{\langle \sum_i \delta\mathbf{v}_i(t) \cdot \delta\mathbf{v}_i(t+\tau) \rangle}{\langle \sum_i \delta\mathbf{v}_i(t) \cdot \delta\mathbf{v}_i(t) \rangle} \tag{9}$$

In this case the angle brackets indicate averaging over different starting time points t. We fit this function by

$$\delta C_{vv}(\tau) = Ae^{-\tau/\tau_0}\cos(\omega\tau) + \kappa \tag{10}$$

where the temporal correlation length is given by τ_0, and A, κ and ω are fit constants with the constraint $A + \kappa = 1$.

Analysis of ciliary beating. The cilia beat frequency and wave velocity were measured from kymographs obtained from time-lapse imaging of ciliary beating. See Supplementary Section 1e for details.

Literature survey of patchiness and coverage fraction. See Supplementary Section 1f and Extended Data Fig. 7.

Simulation. *Fundamental solution.* The fundamental solution of Stokes flow (also known as the Stokeslet or Green's function) in a liquid film was derived recently by Mathijssen and colleagues[34]. The confinement drastically changes the flow structure in these geometries, and therefore we revise the theoretical background of these

hydrodynamics briefly in Supplementary Section 2a. Extended Data Fig. 3 also shows this exact solution as a function of confinement.

Envelope approach. In this Article, we follow an alternative method inspired by the 'envelope approach' introduced by Lighthill[35] and Blake[36] to study ciliary propulsion. Instead of modelling the cilia with point forces, one can consider an envelope that covers the tips of numerous beating cilia that together form a continuous moving sheet. The no-slip condition on the bottom surface is then replaced by the motion of this envelope, $\mathbf{v}_e = U\mathbf{p}$, a tangential slip velocity that follows the orientation field $\mathbf{p}$ of the underlying cilia with an average local flow velocity U. This approximation is justified in the case when the cilia are close together, which is true for multiciliated cells with $N_{\text{cilia}} \approx 200$ cilia.

On the one hand, this approach coarse-grains length scales smaller than the cell, so it cannot resolve the interesting flows around the individual cilia that can give rise to mixing and nutrient exchange[19,22]. On the other hand, it is very tractable analytically (as seen in the study of micro-swimmers and active colloids[37]) and it is straightforward to implement numerically, as is discussed next, being suitable even for very large systems.

CFD solver. The flow velocity $\mathbf{v}(\mathbf{r})$ is simulated using a 3D CFD solver for the incompressible Navier–Stokes equations. Throughout this Article we focus on Newtonian fluids, but in section 'Shear-dependent viscosity' we also consider viscoelastic fluids with a shear-dependent viscosity. The CFD solver is implemented in a custom-built MATLAB code, optimized for low Reynolds numbers by using an implicit Crank–Nicolson method for the viscous terms and an Adams–Bashforth method for the advection terms[38]. This algorithm is implemented on a staggered grid of size $N_x^g \times N_y^g \times N_z^g$ corresponding to a liquid film of size $L_x \times L_y \times H$ (μm) and with periodic boundary conditions in the x and y directions, where x is defined as the D–P direction of the trachea. At the fluid–air interface we enforce the no-shear condition, $\frac{\partial \mathbf{v}}{\partial z} = 0$ at $z = H$. On the tissue surface we apply the no-slip condition in the absence of cilia ($c = 0$), and in the presence of cilia ($c = 1$) we impose a slip velocity set by the envelope model, which gives the boundary condition

$$\mathbf{v}(\mathbf{r}) = cU\mathbf{p} \quad \text{on} \quad z = 0 \tag{11}$$

Here, the cilia distribution $c(\mathbf{r})$ and orientations $\mathbf{p}(\mathbf{r})$ are either taken directly from experiments (section 'Experimental input') or systematically generated in silico for different coverage fractions, wavelengths and disorder (section 'Controlled variations'). We simulate this system until the (unique) solution is reached at steady state, after which we save the 3D velocity field and the pressure field of the ciliary flow.

Total flux and clearance time. Once the flow is solved we compute the total flux in the D–P direction:

$$J = \int_0^H \int_0^{L_y} v_x \mathrm{d}y\mathrm{d}z \tag{12}$$

which, due to incompressibility, is the same for all planes perpendicular to x. Because of this condition, the flux is equivalent to the volume-averaged flow along x, because $\iiint v_x \mathrm{d}x\mathrm{d}y\mathrm{d}z = J\int_0^{L_x} \mathrm{d}x = JL_x$. Using the linearity of the Stokes equations, the flux can also be rewritten as

$$J = \varphi H L_y U \langle p_x \rangle \tag{13}$$

where the coverage fraction is given by $\varphi = \int_0^{L_x}\int_0^{L_y} c(\mathbf{r})\mathrm{d}x\mathrm{d}y/(L_xL_y)$, which is equivalent to equation (M2). We also define the z-averaged flow velocity as $\bar{\mathbf{v}} = \int_0^H \{v_x, v_y\}\mathrm{d}z/H$, the mean longitudinal flow as $\langle \bar{v}_x \rangle = \varphi U \langle p_x \rangle$ and the largest back-flow as $\beta = \min_x \min_y \bar{v}_x$.

Subsequently, the clearance time is obtained by simulating particle trajectories that represent non-motile viruses, bacteria or other harmful pathogens. These particles are subject to the computed flow and also Gaussian fluctuations with diffusivity D. The Stokes–Einstein diffusivity due to thermal noise is $D \approx 10^{-1}\,\mu\text{m}^2\,\text{s}^{-1}$ for micrometre-sized particles in water of viscosity $\mu = 10^{-3}$ Pa s. However, in mucus, the diffusivity is generally smaller than water, $D \approx 10^{-1}$–$10^{-4}\,\mu\text{m}^2\,\text{s}^{-1}$ for micrometre-sized particles, because the mucus is much thicker than water with viscosities of $\mu \approx 0.001$–1 Pa s (ref. [39]).

We run a Brownian dynamics (BD) simulation to find the trajectories for an ensemble of $N_1 \geq 10^3$ particles. Initially the particle positions $\mathbf{r}_p$ are uniformly distributed across the simulation box, and follow the Langevin equation

$$\frac{\partial \mathbf{r}_p}{\partial t} = \bar{\mathbf{v}}(\mathbf{r}_p) + \sqrt{2D}\eta(\mathbf{t}) \tag{14}$$

where the noise is defined by the correlation functions $\langle \eta_i(t) \rangle = 0$ and $\langle \eta_i(t)\eta_j(t') \rangle = \delta(t - t')\delta_{ij}$. The Péclet number is defined as

$$\text{Pé} = \frac{\lambda \varphi U}{D} \tag{15}$$

which is large if the effects of advection outcompete diffusion.

These equations are integrated with a fourth-order Runge–Kutta scheme, again with periodic boundary conditions in the x and y directions. For each pathogen i we then record the time T_i taken to travel a distance L_x in the x direction, along the D–P axis. Hence, we define the clearance time $T_c = \langle T \rangle$ as the first-passage time averaged over an ensemble of N_1 independent particles. We verified that this quantity does not depend on individual initial positions or the simulation geometry. Rather than absolute values, we report a non-dimensional ratio in all figures, such as $\frac{\langle T \rangle(\varphi)}{\langle T \rangle(\varphi=1)}$, to analyse the effect of each parameter.

Importantly, this clearance time is not only a measure of the total flux, but also of the flow structure. In particular, it is a measure of the connectivity between streamlines. If the streamlines are open and connected with the trachea outlet, the larynx, then pathogens will follow the river and be cleared rapidly. If the streamlines are closed, however, the particles are trapped in recirculation zones for a long time. Therefore, even small fluctuations (that is, a large Péclet number) can have a significant effect on the clearance times.

To the best of our knowledge, evaluating streamline connectivity using the first-passage time is a new concept. Having said that, streamline topology is important for transport and percolation in plasma physics[40] and affects particle diffusion in turbulence[41]. Recent results also show that changes in streamline topology can greatly enhance the rate of heat and mass transfer from neutrally buoyant particles in a shear flow[42,43].

Experimental input. In Supplementary Section 2e we provide a detailed description of how exactly the experimental data are implemented in the CFD simulations, both for large-scale and small-scale flows.

Controlled variations. In Supplementary Section 2f we systematically explore how the total flux and clearance time depend on the physical properties of the mucus flow (Fig. 3a,b). One by one, we address (1) the ciliary coverage fraction, (2) the patchiness, (3) Brownian fluctuations, (4) the spatial heterogeneity and (5) the orientational disorder.

Shear-dependent viscosity. We verify the robustness of our results with respect to viscoelastic effects[44] by considering a power-law fluid with a shear-dependent viscosity[45]. Instead of simulating a Newtonian liquid, we generalize the Stokes equations to

$$0 = \boldsymbol{\nabla} \cdot \underline{\underline{S}}, \quad 0 = \boldsymbol{\nabla} \cdot \mathbf{v} \tag{16}$$

where the stress tensor is given by a constitutive equation:

$$\underline{\underline{S}} = -p\underline{\underline{I}} + 2\mu(\dot{\gamma})\underline{\underline{E}} \tag{17}$$

where $\underline{\underline{I}}$ is the identity matrix, and the shear rate is defined as $\dot{\gamma} = \sqrt{2\underline{\underline{E}} : \underline{\underline{E}}}$ in terms of the deformation tensor

$$\underline{\underline{E}} = \frac{(\boldsymbol{\nabla}\mathbf{v}) + (\boldsymbol{\nabla}\mathbf{v})^{\mathrm{T}}}{2} \tag{18}$$

The power law for the shear-dependent viscosity is

$$\mu(\dot{\gamma}) = k\dot{\gamma}^{n-1} \tag{19}$$

where k is a constant relative to the properties of the fluid and the exponent n indicates whether the liquid is shear-thinning ($n < 1$) or shear-thickening ($n > 1$). The Newtonian flow is recovered in the case of $n = 1$. The implementation of this complex fluid in our CDF solver is described in Supplementary Section 2g.

The resulting ciliary flows are shown in Extended Data Fig. 5. We conclude that, if multiciliated cells drive a film of a generalized Newtonian fluid with a shear-dependent viscosity, recirculation still emerges with patchiness, but the particle clearance can still be reduced by disorder. It would be interesting to generalize this further to other viscoelastic constitutive equations that include normal stress differences, a yield stress or memory effects. The deformation of streamlines and recirculation zones could then be larger, which may enhance particle clearance. Indeed, these complex fluids can be implemented using the CFD framework described here, which provides an interesting avenue for future research.

Hexagonal arrays. We test for robustness with respect to ciliary lattice structure by simulating hexagonal arrays of multiciliated cells, as shown in Extended Data Fig. 6 and described in Supplementary Section 2h. Also, we conclude that back-flow (red areas) and streamline recirculation still emerge when the patchiness λ/H is large. This still leads to increased clearance times, which can be reduced with disorder.

Phase diagrams. Finally, we have constructed three phase diagrams to cross-compare the parameters of coverage fraction, patchiness and ciliary orientation. These simulations are described in Supplementary Section 2i.

Reporting Summary. Further information on research design is available in the Nature Research Reporting Summary linked to this Article.

Data availability

The data that support the plots within this paper and other findings of this study are available from the corresponding author upon reasonable request.

Code availability

The computer codes used in this paper are available from the corresponding author upon reasonable request.

References

32. Bangs, F. K., Schrode, N., Hadjantonakis, A.-K. & Anderson, K. V. Lineage specificity of primary cilia in the mouse embryo. *Nat. Cell Biol.* **17**, 113–122 (2015).
33. Mori, N. & Chang, K.-A. *Introduction to mpiv* (2003); http://www.oceanwave.jp/softwares/mpiv
34. Mathijssen, A. J. T. M., Doostmohammadi, A., Yeomans, J. M. & Shendruk, T. N. Hydrodynamics of microswimmers in films. *J. Fluid Mech.* **806**, 35–70 (2016).
35. Lighthill, M. J. On the squirming motion of nearly spherical deformable bodies through liquids at very small Reynolds numbers. *Commun. Pure Appl. Math.* **5**, 109–118 (1952).
36. Blake, J. R. A spherical envelope approach to ciliary propulsion. *J. Fluid Mech.* **46**, 199–208 (1971).
37. Lauga, E. & Powers, T. R. The hydrodynamics of swimming microorganisms. *Rep. Prog. Phys.* **72**, 096601 (2009).
38. Prosperetti, A. & Tryggvason, G. *Computational Methods for Multiphase Flow* (Cambridge Univ. Press, 2009).
39. Lai, S. K., Wang, Y.-Y., Wirtz, D. & Hanes, J. Micro- and macrorheology of mucus. *Adv. Drug Del. Rev.* **61**, 86–100 (2009).
40. Bakunin, O. G. Reconstruction of streamline topology and percolation models of turbulent transport. *Phys. Usp.* **56**, 243 (2013).
41. Goto, S. & Vassilicos, J. Particle pair diffusion and persistent streamline topology in two-dimensional turbulence. *New J. Phys.* **6**, 65 (2004).
42. Subramanian, G. & Koch, D. L. Centrifugal forces alter streamline topology and greatly enhance the rate of heat and mass transfer from neutrally buoyant particles to a shear flow. *Phys. Rev. Lett.* **96**, 134503 (2006).
43. Krishnamurthy, D. & Subramanian, G. Heat or mass transport from drops in shearing flows. Part 2. Inertial effects on transport. *J. Fluid Mech.* **850**, 484–524 (2018).
44. Thornton, D. J., Rousseau, K. & McGuckin, M. A. Structure and function of the polymeric mucins in airways mucus. *Annu. Rev. Physiol.* **70**, 459–486 (2008).
45. Bird, R. B., Armstrong, R. C. & Hassager, O. *Dynamics of Polymeric Liquids. Vol. 1*: *Fluid Mechanics* (Wiley, 1987).

Acknowledgements

This work was supported by funding from the National Science Foundation Center for Cellular Construction (NSF grant no. DBI-1548297), a Human Frontier Science Program Fellowship to A.J.T.M.M. (LT001670/2017) and a Ruth L. Kirschstein National Research Service Award to M.H. (F32HD089639). M.P. acknowledges support from the Keck Foundation. We thank K. Anderson (Sloan Kettering Institute) for providing the Arl13b-mCherry/Centrin-GFP animals used for this study and the Stanford Research Computing Center for providing computational resources and support. We thank W. Gilpin for providing comments on the manuscript.

Author contributions

G.R.R.-S.J., W.M. and M.P. designed the research. G.R.R.-S.J. and M.H. performed the tissue imaging. G.R.R.-S.J. analysed the data. A.J.T.M.M. contributed intellectually to the paper and developed the simulations. G.R.R.-S.J. and A.J.T.M.M. wrote the manuscript. M.H. and L.J. provided key reagents and resources for tissue imaging. All authors edited the final manuscript.

Competing interests

The authors declare no competing interests.

Additional information

Extended data is available for this paper at https://doi.org/10.1038/s41567-020-0923-8.

Supplementary information is available for this paper at https://doi.org/10.1038/s41567-020-0923-8.

Correspondence and requests for materials should be addressed to M.P.

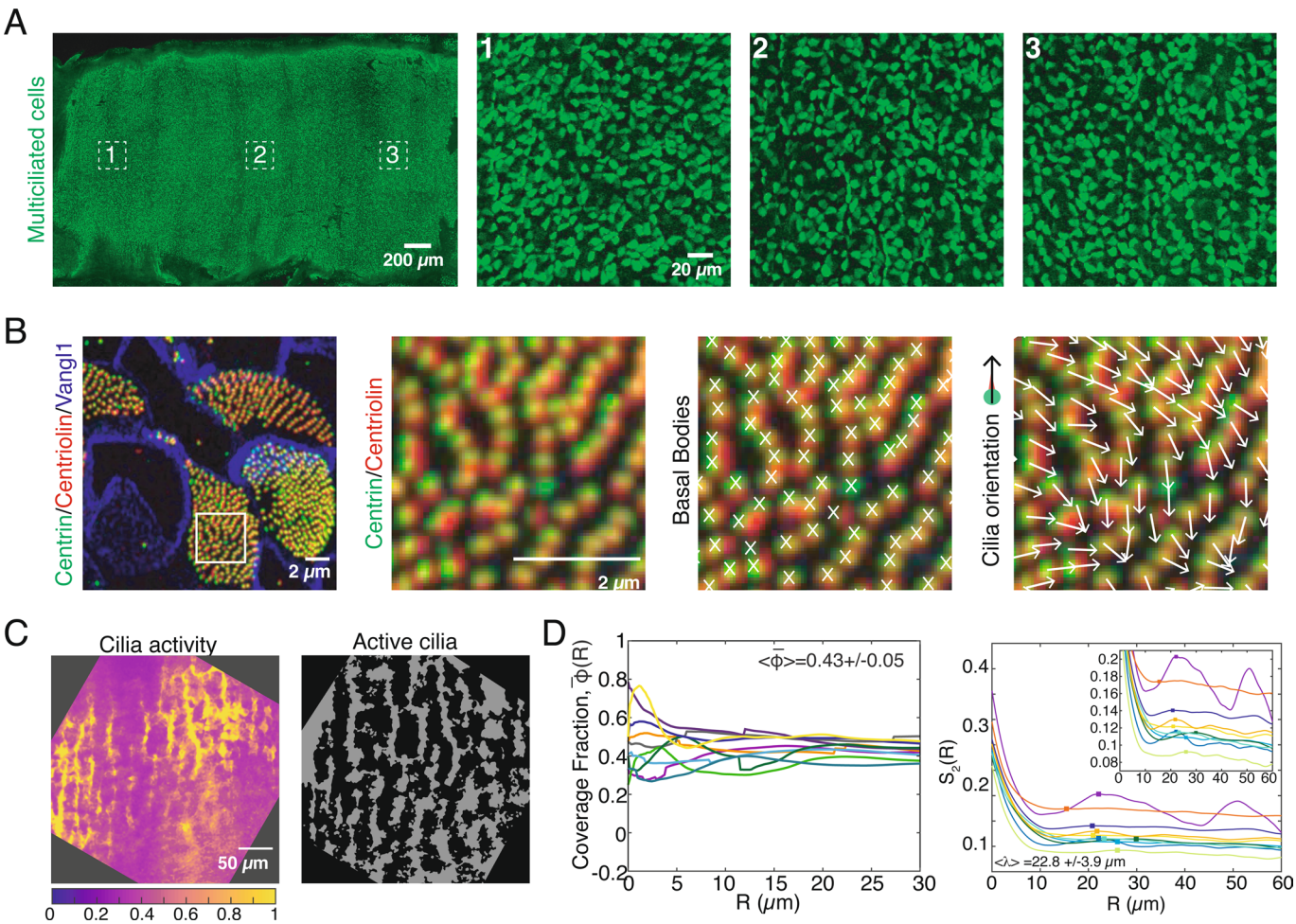

Extended Data Fig. 1 | Quantification of spatial patterning in airway ciliary arrays. A. Immunofluorescence image of a trachea expressing Centrin-GFP (left). Regions outlined by the squares are magnified to the right, showing that multiciliated cells form a 'patchwork' pattern in the distal (1), medial (2) and proximal (3) regions of the trachea. **B**. Illustration of cilia orientation analysis. Individual cilia orientation is measured from pairs of Centrin and Centriolin images. First, individual basal bodies (crossed symbols) are identified from Centrin images. Then the cross-correlation function for a pair of Centrin-Centriolin images is calculated in windows of 50 pixels centered around each basal body. The direction of maximum correlation corresponds to the orientation of each cilium (white arrows). **C**. Heatmap scaled such the 1 corresponds to the regions of maximum cilia activity in Supp. Video 1. Right: Binary image where white regions show regions where cilia are active in Supp. Video 1 (See Methods §2 b). **D**. Coverage fraction and wavelength measured by calculating the spatial correlation function of binary images where regions with cilia activity were identified (e.g. image shown in C).

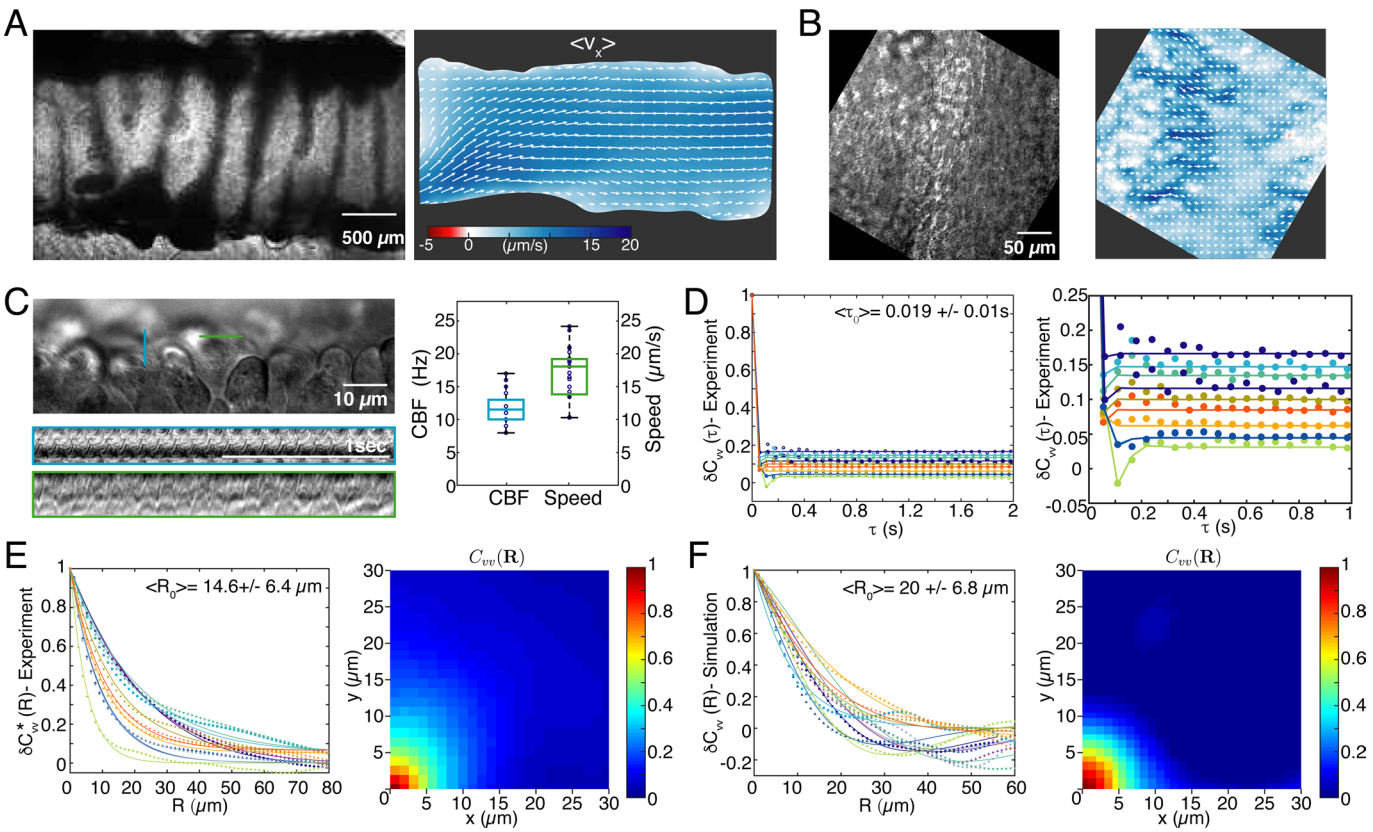

Extended Data Fig. 2 | Quantification of flows generated by airway ciliary arrays. A. Transmitted light image of trachea showing the scale at which flow is measured. Right: Longitudinal flow strength (v_x, red-blue) generated by trachea pictured left. Entire flow strength and streamlines shown in (Fig. 2A,C). **B**. Representative transmitted light image of a typical region of the tissue where flow microstructure is analysed. Right: Longitudinal flow strength (v_x, red-blue) generated by trachea pictured left. Entire flow strength and streamlines shown in (Fig. 2A,C; right). **C**. Quantification of beat frequency and tip velocity of cilia in multiciliated cells. Kymographs drawn from the lines shown in DIC image. Each peak corresponds to one cilia beat cycle (blue), while the slopes of the line indicate the rate at which cilia tips move over time (green). Boxplot central marks indicate the median, and the bottom and top edges of the box indicate the 25th and 75th percentiles, respectively. The whiskers extend to the most extreme data points not considered outliers. **D**. Plot of temporal correlations of the flow field. Plot on the right shows the region where the $\delta C_{vv}(\tau)$ decays, magnified. Each trace is the correlation function M9calculated for a field of view of the size shown in B. Points correspond to values measured, solid line shows exponential fits with an oscillatory component (See Methods §2 d). **E**. Plot of spatial correlations of flow fields measured experimentally. Points correspond to values calculated, solid lines show fits (See Methods §2 d). Right: Heatmap of the two dimensional spatial autocorrelation function $C_{vv}(\mathbf{R})$ for the flow field shown in Fig. 2C (right panel). **F**. Plot of spatial correlations of simulated flow fields. Measurements of multiciliated cell organisation were used as an input for these simulations (See Methods §3 e). Right: Heatmap of the two dimensional spatial autocorrelation function $C_{vv}(\mathbf{R})$ for the simulated flow field shown in Fig. 2D (right panel).

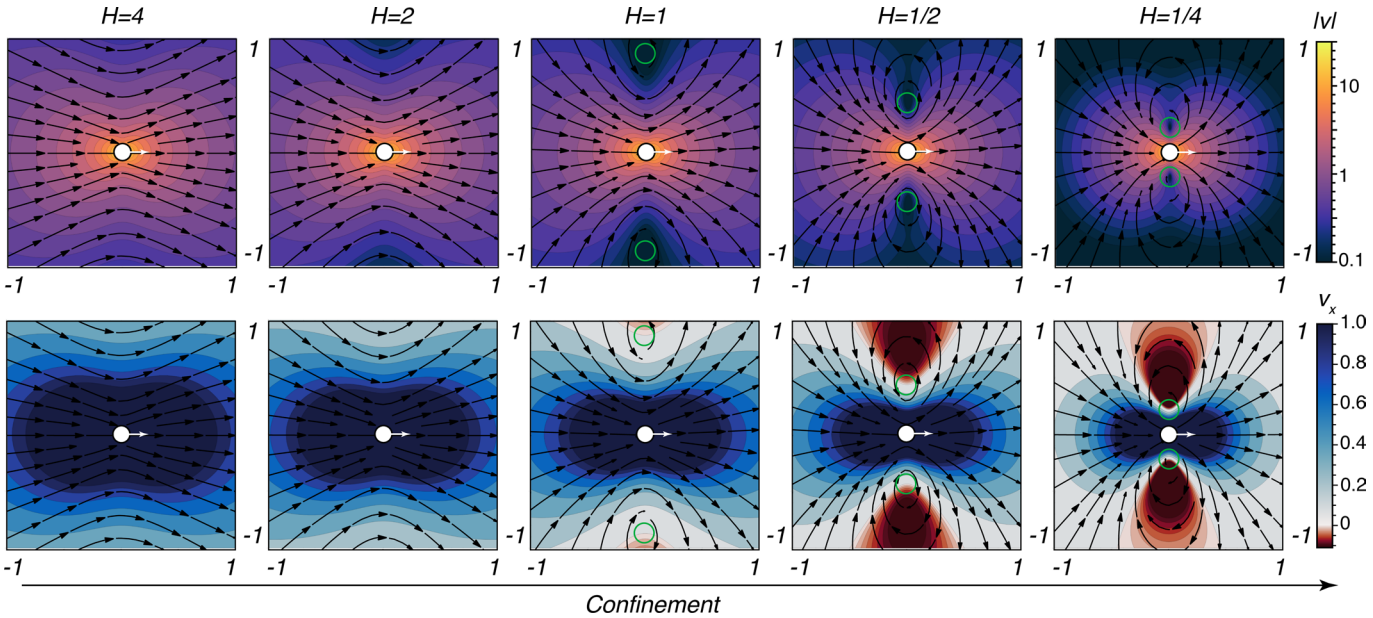

Extended Data Fig. 3 | Effect of confinement on Stokeslet flow in a liquid film. Shown is the analytical solution using 9 image reflections, $(n) = (0) - (9)$ in Table 1 of Mathijssen et al. [34]. The film height in the z direction is H, compared to the horizontal scale $x, y \in [-1, 1]$. The Stokeslets are located in the middle of the film, at $z = H/2$, and oriented in the x direction (white arrows). **T**op panels: Magnitude (thermal) and streamlines (black arrows) of the flow velocity. Bottom panels: Same, showing the x component (red-blue) of the flow. For thin films a recirculation emerges, with a vortex centre marked in green.

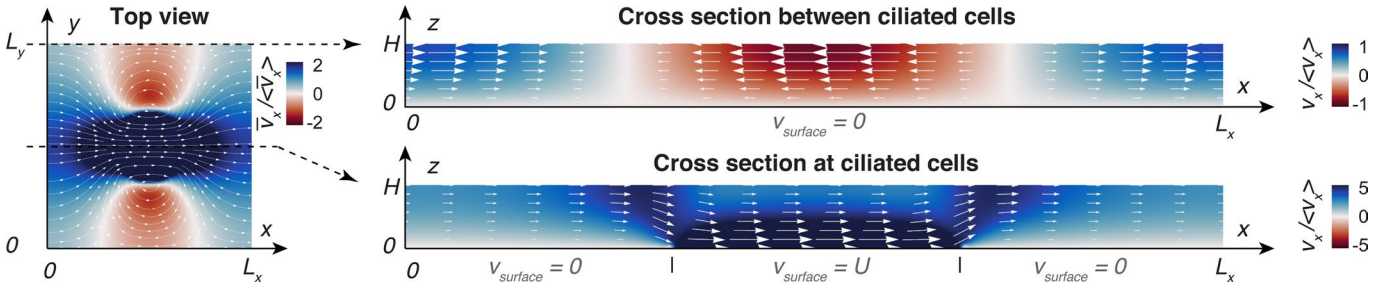

Extended Data Fig. 4 | Three-dimensional structure of the flow generated by a ciliary array. Three-dimensional structure of the flow generated by a ciliary array, simulated for a square lattice with coverage fraction $\phi = 0.1$, patchiness $\lambda/H = 12.8$, crystallinity $\gamma = 1$ and aligned cilia $\langle p_x \rangle = 1$. The wavelength $\lambda = L = 128\mu$m and the film height $H = 10\mu$m. Shown are streamlines (white) and the longitudinal flow strength (red-blue). **L**eft. Top view showing the z-averaged flow velocity, $\bar{\mathbf{v}}$, which is the same as Fig. 3D4. **U**pper right. Cross-section at $y = 0$ or $y = L$, between the ciliated cells. **L**ower right. Cross-section at $y = L/2$, above the ciliated cells.

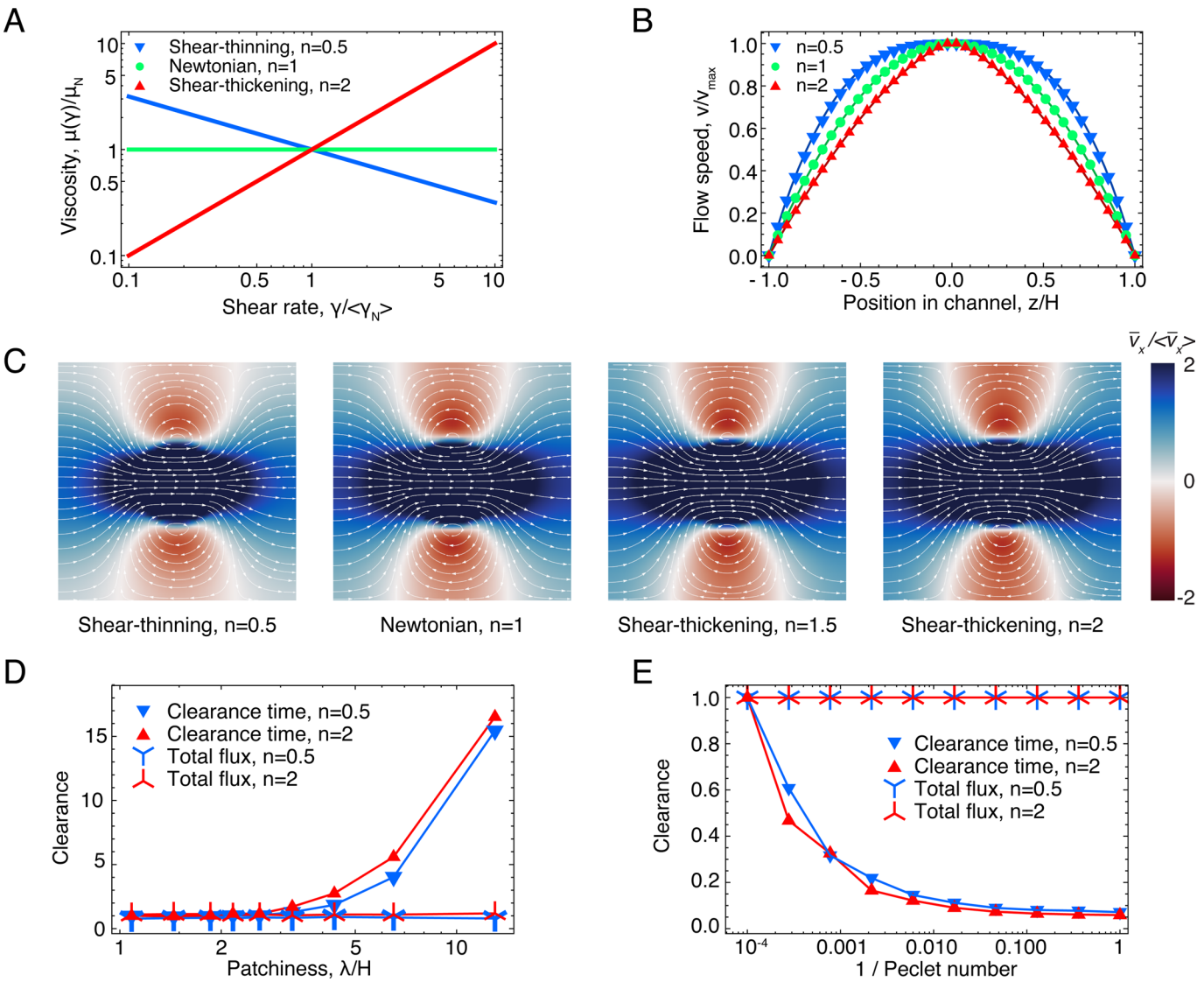

Extended Data Fig. 5 | Effect of shear-dependent viscosity on particle clearance. A. Non-Newtonian viscosity μ as a function of shear rate $\dot{\gamma}$ in a power-law fluid (Eq. M19), for a shear-thinning liquid (blue, $n = 0.5$), a Newtonian liquid (green, $n = 1$) and a shear-thickening liquid (red, $n = 2$). **B**. Channel flow velocity profiles for a power-law fluid. Symbols indicate simulated flows with the CFD solver and lines show the theoretical prediction. For a shear-thinning fluid (blue) the profile is flatter, for a shear-thickening fluid it is sharper (red), and for a Newtonian liquid we recover a parabolic Poiseuille flow. **C**. Flow generated by a ciliary array for different values of the power-law exponent, n, simulated for a square lattice with coverage fraction $\phi = 0.1$, patchiness $\lambda/H = 12.8$, crystallinity $\gamma = 1$ and aligned cilia $\langle p_x \rangle = 1$. Shown are streamlines (white) and the longitudinal flow strength $\bar{v}_x$ normalised with respect to the mean flow $\langle \bar{v}_x \rangle$ of a Newtonian fluid (red-blue), as in Fig. 3D4. **D**. Plot of total flux and clearance time for a shear-thinning (blue) and a shear-thickening fluid (red) as a function of patchiness, normalised with respect to the case of homogeneous coverage ($\lambda = 0$). **E**. Plot of total flux and clearance time for a shear-thinning (blue) and a shear-thickening fluid (red) as a function of Péclet number, normalised with respect to the case of weak noise (Pé $= 10^{-4}$).

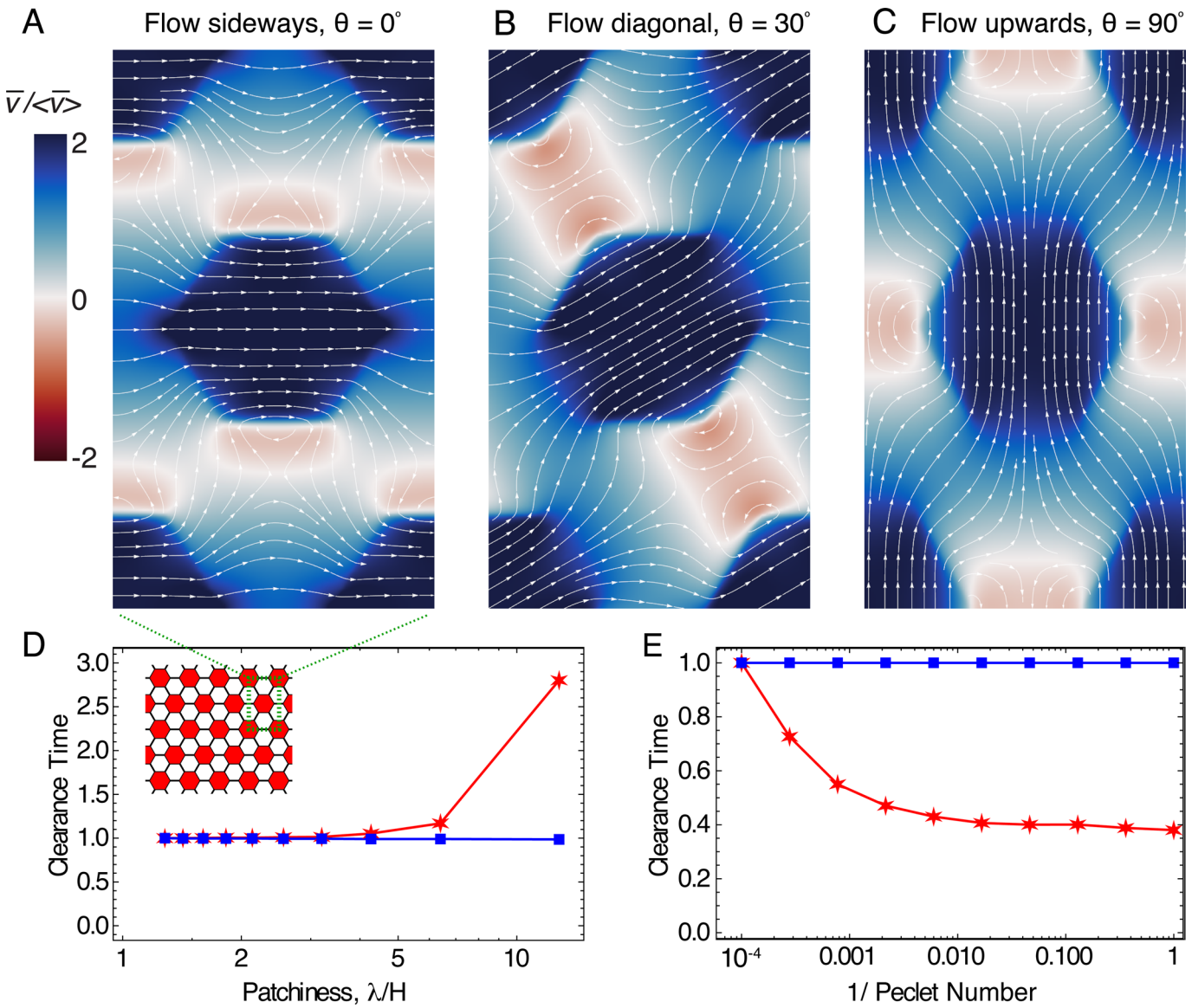

Extended Data Fig. 6 | Total flux and particle clearance for a hexagonal array of ciliary patches. The lattice is shown in the inset of panel D, where red indicates a multiciliated cell. **A**. Simulated flow for cilia oriented in the $\hat{\mathbf{x}}$ direction. Shown are streamlines (white) and the longitudinal flow strength (red-blue). The coverage fraction is $\phi = 0.33$, the patchiness is $\lambda/H = 12.8$, the crystallinity $\gamma = 1$ and the cilia are all aligned $\langle p_x \rangle = 1$. **B**. Same, for cilia oriented in the $\theta = \pi/6$ direction. **C**. Same, for cilia oriented in the $\hat{\mathbf{y}}$ direction. **D**. Plot of total flux (blue) and clearance time (red) as a function of patchiness, for cilia oriented in the $\hat{\mathbf{y}}$ direction, similar to Fig. 3D. **E**. Plot of total flux (blue) and clearance time (red) as a function of Péclet number, for cilia oriented in the $\hat{\mathbf{y}}$ direction, similar to Fig. 4C.

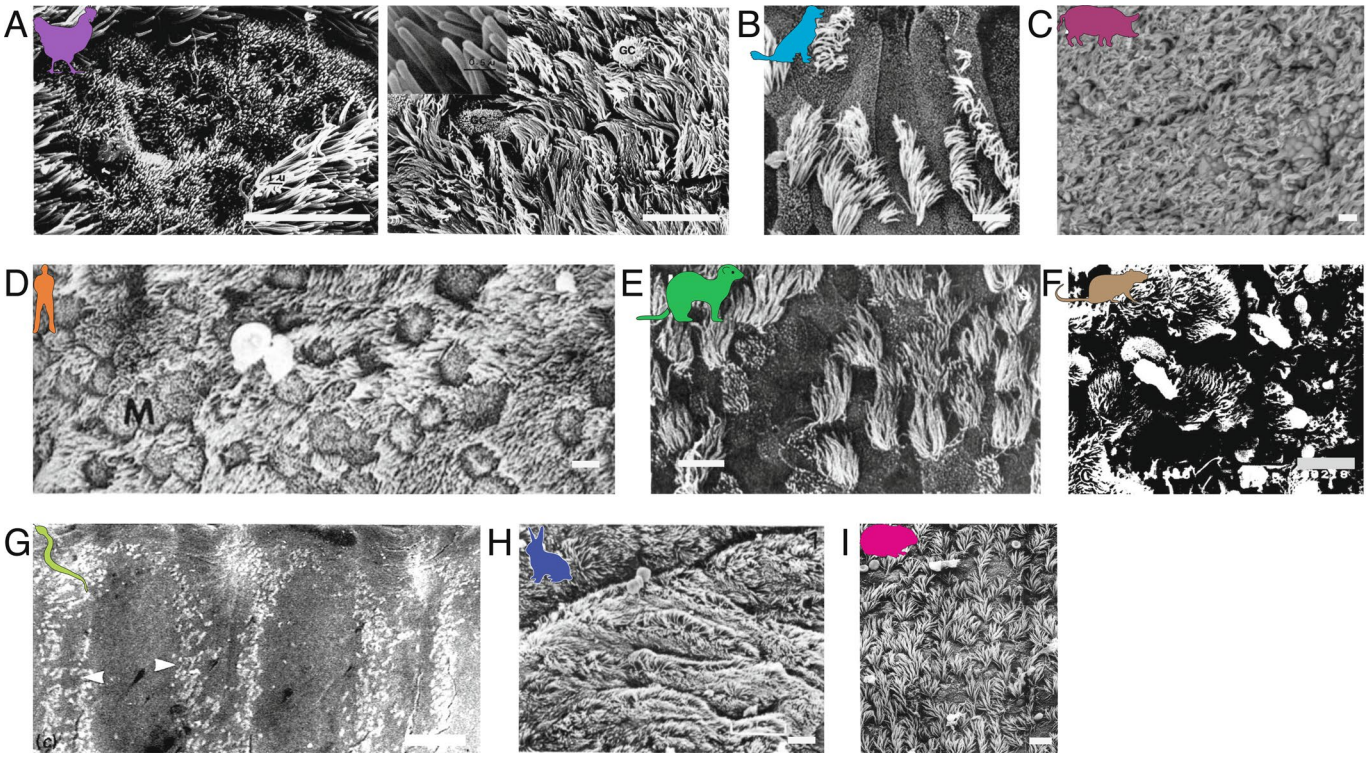

Extended Data Fig. 7 | From the literature: SEM images of airway multiciliated tissue. A. Chicken; Image adapted from[46]. **B**. Dog; Image adapted from[47]. **C**. Pig; Image adapted from[48]. **D**. Human; Image adapted from[49]. **E**. Ferret; Image adapted from[50]. **F**. Rat; Image adapted from[51]. **G**. Snake; Scale bar=100 μm. Image adapted from[52]. **H**. Rabbit; Image adapted from[53]. **I**. Hamster; Image adapted from[54]. Scale bar=10 μm for all panels except G.

46. Lai, M. C. & Ibrahim, A. L. Scanning and transmission electron microscopy of normal chicken tracheal epithelia. *Poultry Sci.* **63**, 1425–1431 (1984).
47. Bemis, D. A. & Kennedy, J. R. An improved system for studying the effect of *Bordetella bronchiseptica* on the ciliary activity of canine tracheal epithelial cells. *J. Infect. Dis.* **144**, 349–357 (1981).
48. ShikKim, W. et al. Tracheal reconstruction with a free vascularized myofascial flap: preclinical investigation in a porcine model to human clinical application. *Sci. Rep.* **7**, 10022 (2017).
49. McDowell, E. M., Barrett, L. A., Glavin, F., Harris, C. & Trump, B. F. The respiratory epithelium. I. Human bronchus. *J. Natl Cancer Inst.* **61**, 539–549 (1978).
50. Leigh, M. et al. Postnatal development of tracheal surface epithelium and submucosal glands in the ferret. *Exp. Lung Res.* **10**, 153–169 (1986).
51. Yu, S. M. & Lin, K. H. Scanning electron microscopy of capsaicin-pretreated trachea in the rat during postnatal development. *Histol. Histopathol.* **10**, 853–860 (1995).
52. Pastor, L. M. A morphological study of the tracheal epithelium of the snake *Natrix maura*. *J. Anatomy* **172**, 47–57 (1990).
53. Sanderson, M. & Sleigh, M. Ciliary activity of cultured rabbit tracheal epithelium: beat pattern and metachrony. *J. Cell Sci.* **47**, 331–347 (1981).
54. Satir, P. & Dirksen, E. R. *Function–Structure Correlations in Cilia from Mammalian Respiratory Tract* 473–494 (American Cancer Society, 2011).

nature research

Corresponding author(s): Manu Prakash

Last updated by author(s): Mar 4, 2020

Reporting Summary

Nature Research wishes to improve the reproducibility of the work that we publish. This form provides structure for consistency and transparency in reporting. For further information on Nature Research policies, see Authors & Referees and the Editorial Policy Checklist.

Statistics

For all statistical analyses, confirm that the following items are present in the figure legend, table legend, main text, or Methods section.

n/a	Confirmed
☐	☒ The exact sample size (*n*) for each experimental group/condition, given as a discrete number and unit of measurement
☐	☒ A statement on whether measurements were taken from distinct samples or whether the same sample was measured repeatedly
☒	☐ The statistical test(s) used AND whether they are one- or two-sided *Only common tests should be described solely by name; describe more complex techniques in the Methods section.*
☒	☐ A description of all covariates tested
☒	☐ A description of any assumptions or corrections, such as tests of normality and adjustment for multiple comparisons
☐	☒ A full description of the statistical parameters including central tendency (e.g. means) or other basic estimates (e.g. regression coefficient) AND variation (e.g. standard deviation) or associated estimates of uncertainty (e.g. confidence intervals)
☒	☐ For null hypothesis testing, the test statistic (e.g. *F*, *t*, *r*) with confidence intervals, effect sizes, degrees of freedom and *P* value noted *Give P values as exact values whenever suitable.*
☒	☐ For Bayesian analysis, information on the choice of priors and Markov chain Monte Carlo settings
☒	☐ For hierarchical and complex designs, identification of the appropriate level for tests and full reporting of outcomes
☒	☐ Estimates of effect sizes (e.g. Cohen's *d*, Pearson's *r*), indicating how they were calculated

Our web collection on statistics for biologists contains articles on many of the points above.

Software and code

Policy information about availability of computer code

Data collection	Data were collected using ImageJ and ZEN (Zeiss) software.
Data analysis	All data analysis was performed using custom written codes in Matlab

For manuscripts utilizing custom algorithms or software that are central to the research but not yet described in published literature, software must be made available to editors/reviewers. We strongly encourage code deposition in a community repository (e.g. GitHub). See the Nature Research guidelines for submitting code & software for further information.

Data

Policy information about availability of data

All manuscripts must include a data availability statement. This statement should provide the following information, where applicable:

- Accession codes, unique identifiers, or web links for publicly available datasets
- A list of figures that have associated raw data
- A description of any restrictions on data availability

All source data and computer codes used in this study are available from the corresponding author upon request.

Field-specific reporting

Please select the one below that is the best fit for your research. If you are not sure, read the appropriate sections before making your selection.

☒ Life sciences ☐ Behavioural & social sciences ☐ Ecological, evolutionary & environmental sciences

For a reference copy of the document with all sections, see nature.com/documents/nr-reporting-summary-flat.pdf

Life sciences study design

All studies must disclose on these points even when the disclosure is negative.

Sample size	No sample size calculation was performed. Sample sizes were chosen based on standard sample sizes used when working with vertebrate animals. The sample sizes used were deemed sufficient since measurements were consistent in independent animals and tissue sections and across experiments performed on different days.
Data exclusions	Dissected tissues were ciliary activity was not observed or diminished though time were excluded from this study. This criteria was implemented since diminished cilia activity is an indication of tissue damage. This criteria was determined before data analysis.
Replication	Experiments carried out in different biological replicates and tissue regions through different days were reproducible.
Randomization	This is not relevant to the study since all the mice are considered to be part of one experimental group.
Blinding	Blinding is not relevant to the study since all mice are part of one experiemental group.

Reporting for specific materials, systems and methods

We require information from authors about some types of materials, experimental systems and methods used in many studies. Here, indicate whether each material, system or method listed is relevant to your study. If you are not sure if a list item applies to your research, read the appropriate section before selecting a response.

Materials & experimental systems

n/a	Involved in the study
☐	☒ Antibodies
☒	☐ Eukaryotic cell lines
☒	☐ Palaeontology
☐	☒ Animals and other organisms
☒	☐ Human research participants
☒	☐ Clinical data

Methods

n/a	Involved in the study
☒	☐ ChIP-seq
☒	☐ Flow cytometry
☒	☐ MRI-based neuroimaging

Antibodies

Antibodies used	mouse monoclonal anti-Centriolin, Santa Cruz: sc-365521; rabbit anti-Vangl1, Sigma: HPA025235; Alexa Fluor 594-goat anti-rabbit and Alexa 633-donkey anti-mouse, Invitrogen
Validation	Am. J. Hum. Genet. 104: 229-245. Methods Cell Biol. 2015;127:37-54. doi: 10.1016/bs.mcb.2015.01.016

Animals and other organisms

Policy information about studies involving animals; ARRIVE guidelines recommended for reporting animal research

Laboratory animals	Arl13b-mCherry; Centrin2-GFP (JAX 027967) mouse
Wild animals	Study does not involve wild animals
Field-collected samples	Study did not involve samples collected from the field
Ethics oversight	All protocols were approved by the University of California San Francisco Institutional Animal Care and Use Committee

Note that full information on the approval of the study protocol must also be provided in the manuscript.